Analyzing the turbulent Planetary Boundary Layer by remote sensing systems: Doppler wind lidar, aerosol elastic lidar and microwave radiometer

Gregori de Arruda Moreira[1,2,3], Juan Luis Guerrero-Rascado[1,2], Jose A. Benavent-Oltra[1,2], Pablo Ortiz-Amezcua[1,2], Roberto Román[1,2,4], Andrés E. Bedoya-Velásquez[1,2,5] Juan Antonio Bravo-Aranda[1,2], Francisco Jose Olmo Reyes[1,2], Eduardo Landulfo[3], Lucas Alados-Arboledas[1,2]

[1]Andalusian Institute for Earth System Research (IISTA-CEAMA), Granada, Spain
[2]Dpt. Applied Physics, University of Granada, Granada, Spain
[3]Institute of Research and Nuclear Energy (IPEN), São Paulo, Brazil
[4]Grupo de Óptica Atmosférica (GOA), Universidad de Valladolid, Valladolid, Spain.
[5]Sciences Faculty, Department of Physics, Universidad Nacional de Colombia, Medellín, Colombia.

Correspondence to: Gregori de Arruda Moreira (gregori.moreira@usp.br)

Abstract

The Planetary Boundary Layer (PBL) is the lowermost region of troposphere and endowed with turbulent characteristics, which can have mechanical and/or thermodynamic origins. Such behavior gives to this layer great importance, mainly in studies about pollutant dispersion and weather forecasting. However, the instruments usually applied in studies about turbulence in the PBL have limitations in spatial resolution (anemometer towers) or temporal resolution (instrumentation onboard aircraft). Ground-based remote sensing, both active and passive, offers an alternative for studying the PBL. In this study we show the capabilities of combining different remote sensing systems (microwave radiometer [MWR], Doppler lidar [DL] and elastic lidar [EL]) for retrieving a detailed picture on the PBL turbulent features. The statistical moments of the high frequency distributions of the vertical wind velocity, derived from DL and of the backscattered coefficient derived from EL, are corrected by two methodologies, namely first lag and -2/3 correction. The corrected profiles, obtained from DL data, present small differences when compared against the uncorrected profiles, showing the low influence of noise and the viability of the proposed methodology. Concerning EL, in addition to analyze the influence of noise, we explore the use of different wavelengths that usually include EL systems operated in extended networks, like EARLINET, LALINET, MPLNET or SKYNET. In this way we want to show the feasibility of extending the capability of existing monitoring networks without strong investments or changes in their measurements protocols. Two case studies were analyzed in detail, one corresponding to a well-defined PBL and another one corresponding to a situation with presence of a Saharan dust lofted aerosol layer and clouds. In both cases we discuss results provided by the different instruments showing their complementarity and the cautions to be applied in the data interpretation. Our study shows that the use of EL at 532nm requires a careful correction of the signal using the first lag time correction in order to get reliable turbulence information on the PBL.

Keywords: Turbulence, Planetary Boundary Layer, Doppler lidar, elastic lidar, microwave radiometer, Earlinet.

1 Introduction

The Planetary Boundary Layer (PBL) is the atmospheric layer directly influenced by the Earth's surface that responds to its changes within time scales around an hour (Stull, 1988). Such layer is located at the lowermost region of troposphere, and is mainly characterized by turbulent processes and a daily evolution cycle. In an ideal situation, instants after sunrise, ground surface temperature increase due to the positive net radiative flux (R_n). This process intensifies the convection, thus, the ascending warm air masses heat the air masses aloft, originating the Convective Boundary Layer (CBL) or Mixing Layer (ML), which has this name due to a mixing process generated by this turbulent ascending air parcels. Slightly before sunset the gradual reduction of incoming solar irradiance at the Earth's surface causes the decrease of the positive R_n and its change in sign. In this situation, there is a reduction of the convective processes and a weakening of the turbulence. In this process the CBL leads to the development of two layers, namely a stably stratified boundary layer called Stable Boundary Layer (SBL) close to the surface, and the Residual Layer (RL) that contains features from the previous day's ML and is just above the SBL.

Knowledge of the turbulent processes in the CBL is important in diverse studies, mainly for atmospheric modeling and pollutant dispersion, since turbulent mixing can be considered as the primary process by which aerosol particles and other scalars are transported vertically in atmosphere. Because turbulent processes are treated as nondeterministic, they are characterized and described by their statistical properties (high order statistical moments). When applied to atmospheric studies such analysis provide information about the field of turbulent fluctuation, as well as, a description of the mixing process in the PBL (Pal et al., 2010).

Anemometer towers have been widely applied in studies about turbulence (e.g., Kaimal and Gaynor, 1983; van Ulden and Wieringa, 1996), however the limited vertical range of these equipment restrict the analysis to regions close to surface. Aircraft have also been used in atmospheric turbulence studies (e.g., Lenschow et al., 1980; Williams and Hacker, 1992; Lenschow et al., 1994; Albrecht et al., 1995; Stull et al., 1997; Andrews et al., 2004; Vogelmann et al., 2012), nevertheless their short time window limits the analysis. In this scenario, systems with high spatial and temporal resolution and enough range are necessary in order to provide more detailed results along the day throughout the whole thickness of the PBL.

In the last decades, lidar systems have been increasingly applied in this kind of study due to their large vertical range, high data acquisition rate and capability to detect several observed quantities such as vertical wind velocity [Doppler lidar] (e.g. Lenschow et al., 2000; Lothon et al., 2006; O'Connor et al., 2010), water vapor [Raman lidar and DIAL] (e.g. Wulfmeyer, 1999; Kiemle et al., 2007; Wulfmeyer et al., 2010; Turner et al., 2014; Muppa et al., 2015), temperature [rotational Raman lidar] (e.g. Behrendt et al., 2015) and aerosol [elastic lidar] (e.g. Pal et al., 2010; McNicholas et al., 2015). This allows the observation of a wide range of atmospheric processes. For example, Pal et al. (2010) demonstrated how the statistical analyses obtained from high-order moments of elastic lidar can provide information about aerosol plume dynamics in the PBL region. In addition, when different lidar systems operate synergistically, as for example in Engelmann et al. (2008), who combined elastic and Doppler lidar data, it is possible to identify very complex variables such as vertical particle flux.

Different works (Ansmann et al., 2010; O'Connor et al., 2010) have evidenced the feasibility for characterizing the PBL turbulence by DL. Pal et al. (2010) have shown the feasibility for retrieving information on the PBL turbulenc from high high-order moments of elastic lidar operating at 1064. Such approaches are even more attractive when considering facilities of networks, e. g. European Aerosol Research Lidar NETwork (EARLINET) (Pappalardo et al., 2014), Microwave Radiometer Network (MWRNET) (Rose et al., 2005; Caumont et al., 2016) and ACTRIS CLOUDNET (Illingworth et al., 2007). For these reasons, and having in mind the wide spread of elastic lidar systems operated at other wavelengths, like 532 nm or 355 nm, it would be worthy test the feasibility of these other wavelengths in the characterization of the PBL turbulent behavior.

The use of simple techniques, applied to the aforementioned remote systems provide robust and similar information on the convective PBL height, $PBLH$ (see for example Moreira et al, 2018), or a complementary information when the CBL is substituted by the presence of the SBL and the RL (Moreira et al., in preparation). Thus, the combination of information obtained from the active remote sensing systems, DL and EL, acquired with a temporal resolution close to 1 s, and that provided by MWR can provide a detailed understanding about different features of the PBL, like structure (CBL versus SBL and RL), height of the layers, rate of growth of the $PBLH$ and turbulence.

In this study we show the feasibility of obtaining a clear insight on the PBL behavior using a combination of active and passive remote sensing systems (Elastic Lidar [EL], Doppler Lidar [DL] and Microwave Radiometer [MWR]) acquired during the SLOPE-I campaign, held at IISTA-CEAMA (Andalusian Institute for Earth System Research, Granada, Spain) from May to August 2016. One of the goals is to show the feasibility of using EL at 532 nm, considering the larger realibility of the measurements at this wavelength.

This paper is organized as follows. Description of the experimental site and the equipment setup are presented in Section 2. The methodologies applied are introduced in Section 3. Section 4 presents the results of the analyses using the different methodologies. Finally, conclusions are summarized in Section 5.

2 Experimental site and instrumentation

The SLOPE-I (Sierra nevada Lidar aerOsol Profiling Experiment) campaign was performed from May to September 2016 in South-Eastern Spain in the framework of the European Research Infrastructure for the observation of Aerosol, Clouds, and Trace gases (ACTRIS). The main objective of this campaign was to perform a closure study by comparing remote sensing system retrievals of atmospheric aerosol properties, using remote systems operating at the Andalusian Institute of Earth System Research (IISTA-CEAMA) and in-situ measurements operating at different altitudes in the Northern slope of Sierra Nevada, around 20 km away from IISTA-CEAMA (Bedoya-Velásquezet al., 2018; Román et al., 2018). The IISTA-CEAMA station is part of EARLINET (Pappalardo et al, 2014) since 2005 and at present is an ACTRIS station (http://actris2.nilu.no/). The research facilities are located at Granada, a medium size city in Southeastern Spain (Granada, 37.16°N, 3.61°W, 680 m a.s.l.), surrounded by mountains and with Mediterranean-

continental climate conditions that are responsible for cool winters and hot summers. Rain is scarce, especially from late spring to early autumn. Granada is affected by different kind of aerosol particles locally originated and medium-long range transported from Europe, Africa and North America (Lyamani et al., 2006; Guerrero-Rascado et al., 2008, 2009; Titos et al., 2012; Navas-Guzmán et al., 2013; Valenzuela et al., 2014, Ortiz-Amezcua et al, 2014, 2017).

MULHACEN is a biaxial ground-based Raman lidar system operated at IISTA-CEAMA in the frame of EARLINET research network. This system operates with a pulsed Nd:YAG laser, frequency doubled and tripled by Potassium Dideuterium Phosphate crystals, emitting at wavelengths of 355, 532 and 1064 nm with output energies per pulse of 60, 65 and 110 mJ, respectively. MULHACEN operates with three elastic channels: 355, 532 (parallel and perpendicular polarization) and 1064 nm and three Raman-shifted channels: 387 (from N_2), 408 (from H_2O) and 607 nm (from N_2). MULHACEN's overlap is complete at 90% between 520 and 820 m a.g.l. for all the wavelengths, reaching full overlap around 1220 m a.g.l. (Navas-Guzmán et al ., 2011; Guerrero-Rascado et al. 2010). Calibration of the depolarization capabilities is done following Bravo-Aranda et al. (2013). This system was operated with a temporal and spatial resolution of 2 s and 7.5 m, respectively. More details can be found at Guerrero-Rascado et al. (2008, 2009).

The Doppler lidar (Halo Photonics, model Stream Line XR) is also operated at IISTA-CEAMA. This system works in continuous and automatic mode from May 2016. It operates at 1.5 μm with pulse energy and repetition rate of 100 μJ and 15 KHz, respectively. This system record the backscattered signal with 300 gates, being the range gate length 30 m, with the first gate at 60 m. The telescope focus is set to approximately 800 m. For this work the data were collected in stare mode (laser beam is pointed at vertical with respect to the ground surface) with a time resolution of 2 s.

Furthermore, we operated the ground-based passive microwave radiometer (RPG-HATPRO G2, Radiometer Physics GmbH), which is member of the MWRnet [http://cetemps.aquila.infn.it/mwrnet/]. This system operates in automatic and continuous mode at IISTA-CEAMA since November 2011. The microwave radiometer (MWR) measures the sky brightness temperature with a radiometric resolution between 0.3 and 0.4 K root mean square error at 1 s integration time, using direct detection receivers within two bands: K-band (water vapor – frequencies: 22.24 GHz, 23.04 GHz, 23.84 GHz, 25.44 GHz, 26.24 GHz, 27.84 GHz, 31.4 GHz) and V-band (oxygen – frequencies: 51.26 GHz, 52.28 GHz, 53.86 GHz, 54.94 GHz, 56.66 GHz, 57.3 GHz, 58.0 GHz). From these bands is possible to obtain profiles of water vapor and temperature, respectively, by inversion algorithms described in Rose et al. (2005). The range resolution of these profiles vary between 10 and 200 m in the first 2 km and between 200 and 1000 m in the layer between 2 and 10 km (Navas-Guzmán et al., 2014).

The meteorological sensor (HMP60, Vaisala) is used to register the air surface temperature and surface relative humidity, with a temporal resolution of 1 minute. Relative humidity is monitored with an accuracy of ± 3%, and air surface temperature is acquired with an accuracy and precision of 0.6º C and 0.01º C, respectively.

A CM-11 pyranometer manufactured by Kipp&Zonen (Delft, The Netherlands) is also installed in the ground-based station. This equipment measures the shortwave (SW) solar global horizontal irradiance data

(305–2800 nm). The CM-11 pyranometer complies with the specifications for the first-class WMO (World Meteorological Organization) classification of this instrument (resolution better than ±5 Wm^{-2}), and the calibration factor stability has been periodically checked against a reference CM-11 pyranometer (Antón et. al, 2012).

3 Methodology

3.1 MWR data analysis

The MWR data are analyzed combining two algorithms, Parcel Method [PM] (Holzworth, 1964) and Temperature Gradient Method [TGM] (Coen, 2014), in order to estimate the PBL Height ($PBLH_{MWR}$) in convective and stable situations, respectively. The different situations are discriminated by comparing the surface potential temperature ($\theta(z_0)$) with the corresponding vertical profile of $\theta(z)$ up to 5 km. Those cases where all the points in the vertical profile have values larger than $\theta(z_0)$ are labeled as stable, and TGM is applied. Otherwise the situation is labeled as unstable and the PM is applied. The vertical profile of $\theta(z)$ is obtained from the vertical profile of T(z) using the following equation (Stull, 2011):

$$\theta(z) = T(z) + 0.0098 * z \quad (1)$$

where $T(z)$ is the temperature profile provided by MWR, z is the height above the sea level, and 0.0098 K/m is the dry adiabatic temperature gradient. A meteorological station co-located with the MWR is used to detect the surface temperature [$T(z_0)$]. In order to reduce the noise, $\theta(z)$ profiles were averaged providing a $PBLH_{MWR}$value at 30 minutes intervals. This methodology of $PBLH$detection was selected as the reference due to the results obtained during a performed campaign of comparison between MWR and radiosonde data, where twenty-three radiosondes were launched. High correlations were found between $PBLH$ retrievals provided by both instruments in stable and unstable cases. Further details are given by Moreira et al. (2018a).

3.2 Lidar retrieval of the PBLH.

The simple processing of DL and EL data allow to estimate the CBL height. Moreira et al. (2018), have discussed this issue in depth, while Moreira et al. (in preparation) have exploited the complementarity of the data obtained from distinct remote sensing systems in order to distinguish the sublayers during the period when the SBL and RL substitute the CBL, as well as, in complex situations, like as, presence of dust layers.

The $PBLH$ obtained from DL data ($PBLH_{Doppler}$) is estimated from variance threshold method. In this method the $PBLH_{Doppler}$is attributed to height where σ_w^2 is higher than a determinate threshold, which was adopted as 0.16 m^2/s^2 (Moreira et al., 2018a). For the $PBLH_{Doppler}$ calculations was selected a time interval of 30 minutes. In concerning the $PBLH$ obtained from EL ($PBLH_{Elastic}$), the variance method is applied.

Such method assumes the maximum of σ^2_{RCS} as $PBLH_{Elastic}$ (Moreira et al., 2015). The σ^2_{RCS} is obtained from a time interval of 30 minutes.

3.3 Lidar turbulence analysis

Both lidar systems, DL and EL, gathered data with a temporal resolution of 2 seconds. Then, the data are averaged in 1-hour packages, from which the mean value is extracted $[\acute{q}(z)]$. Such mean value is subtracted from each $q(z,t)$ profile in order to estimate the vertical profile of the fluctuation for the measured variable $[q'(z,t)]$ (i.e. vertical velocity for the DL):

$$q'(z,t) = q(z,t) - \bar{q}(z) \quad (2)$$

Then, from $q'(z,t)$ is possible to obtain the high-order moments (variance (σ^2), skewness (S) and kurtosis (K)), as well as, the integral time scale (τ - which isthe time over which the turbulent process are highly correlated to itself) as shown in Table 1. These variables can also be obtained from the following autocovariance function, M_{ij}:

$$M_{ij} = \int_0^{t_f} [q'(z,t)]^i [q'(z,t+t_f)]^j dt \quad (3)$$

where t_f is the final time, i and j indicate the order of autocovariance function.

However, it is necessary to considerer that the acquired real data contain instrumental noise, $\varepsilon(z)$. Therefore, the equation 3 can be rewritten as:

$$M_{ij} = \int_0^{\tau} [q(z,t) + \varepsilon(z,t)]^i [q(z,t+\tau) + \varepsilon(z,t+\tau)]^j dt \quad (4)$$

The autocovariance function of a time series with zero lag results in the sum of the variances of the atmospheric variable and its $\varepsilon(z)$. Nevertheless, atmospheric fluctuations are correlated in time, but the $\varepsilon(z)$ is random and uncorrelated with the atmospheric signal. Consequently, the noise is only associated with lag 0 (Fig. 1). Based on this concept Lenschow et al. (2000) suggested to obtain the corrected autocovariance function, $M_{11}(\rightarrow 0)$, from two methods, namely first lag correction or -2/3 law correction. In the first method, $M_{11}(\rightarrow 0)$ is obtained directly by the subtraction of lag 0, $\Delta M_{11}(0)$, from the autocovariance function, $M_{11}(0)$. In the second method $M_{11}(\rightarrow 0)$ is generated by the extrapolation of $M_{11}(0)$ at firsts nonzero lags back to lag zero (-2/3 law correction). The extrapolation can be performed using the inertial subrange hypothesis, which is described by the following equation (Monin and Yaglom, 1979):

$$M_{11}(\rightarrow 0) = \overline{q'^2(z,t)} + Ct^{2/3} (5)$$

where C represents a parameter of turbulent eddy dissipation rate. The high-order moments and τ corrections and errors are shown in Table 1 (columns 2 and 3, respectively).

The same procedure of analysis is applied in studies with DL and EL, being the main difference the tracer used by each system, which are the fluctuation of vertical wind speed (w') for DL and aerosol number density (N') for EL. DLprovides$w(z,t)$ directly, and therefore the procedure described in Figure 2 can be directly applied. Thus, the two corrections described above are applied separately and finally τ and high-order moments with and without corrections can be estimated.

On the other hand, the EL does not provide $N(z,t)$ directly. Under some restrictions, it is possible to ignore the particle hygroscopic growth and to assume that the vertical distribution of aerosol type does not changes with time, and to adopt the following relation (Pal et al., 2010):

$$\beta_{par}(z,t) \approx N(z,t)Y(z) \Rightarrow \beta'_{par}(z,t) = N'(z,t) \quad (6)$$

where β_{par} and β'_{par} represent the particle backscatter coefficient and its fluctuation, respectively, and $Y(z)$ does not depends on time.

Considering the lidar equation:

$$P_\lambda(z) = P_0 \frac{ct_d}{2} AO(z) \frac{\beta_\lambda(z)}{z^2} e^{-2\int_0^z \alpha_\lambda(z'dz')} \quad (7)$$

where $P_\lambda(z)$ is the signal returned from distance z at time t, z is the distance [m] from the lidar of the volume investigated in the atmosphere, P_0 is the power of the emitted laser pulse, c is the light speed [m/s], t_d is the duration of laser pulse [ns], A is the area [m²] of telescope cross section, $O(z)$ is the overlap function, $\alpha_\lambda(z)$ is the total extinction coefficient (due to atmospheric particles and molecules) [$(km)^{-1}$] at distance z, $\beta_\lambda(z)$ is the total backscatter coefficient (due to atmospheric particles and molecules) [$(km \cdot sr)^{-1}$] at distance z and the subscript λ represents the wavelength. The two path transmittance term related to $\alpha(z)$ is considered as nearly negligible at 1064 nm (Pal et al., 2010). Thus, it is possible to affirm that:

$$RCS_{1064}(z) = P(z)_{1064}.z^2 \cong G.\beta_{1064}(z) \quad (8)$$

and consequently:

$$RCS'_{1064}(z,t) \cong \beta'_{1064}(z,t) = \beta'_{par}(z,t) = N'(z,t) \quad (9)$$

where RCS_{1064} and RCS'_{1064} are the range corrected signal and its fluctuation, respectively, G is a constant and the subscripts represent the wavelength.

In this way, Pal et al. (2010) have shown the feasibility of using EL operating at 1064 nm for describing the atmospheric turbulence. However, having in mind the more extended use of lidar systems based on laser emission at 532 nm in different coordinated networks, e.g., in EARLINET and LALINET (Latin American LIdar NETwork) around 76% and 45% of the systems include the wavelength of 1064 nm, while 95% of the EARLINET systems and 73% of the LALINET systems operate systems that include the wavelength 532 nm (Guerrero-Rascado et al., 2016), in this study we perform the validation of the RCS_{532} in analyses about turbulence using EL, following the procedure described in Figure 3, which is basically the same methodology described earlier for DL.

4 Results

4.1 Error Analysis

The influence of random error in noisy observations rapidly grows for higher-order moments (i.e., the influence of random noise is much larger for the fourth-order moment than for the third-order moment). Therefore, the first step, in order to ascertain the applied methodology and our data quality, we performed the error treatment of DL data as described in Figure 2. For the DL analysis we selected the period 08-09 UTC of 19th May, the same day that will be presented in Case Study 1. This day is characterized by a well-defined PBL.

Figure 4 illustrates the autocovariance function, generated from w', at three different heights. As mentioned before, the lag 0 is contaminated by noise (ε), and thus the impact of the ε increases together with height, mainly above $PBLH_{MWR}$ (1100 m a.g.l. in our example).

Figure 5-A illustrates the comparison between integral time scale ($\tau_{w\prime}$) without correction and the two corrections cited in section 3.2. Except for the first height-bins, under the $PBLH_{MWR}$ the profiles have little differences, as well as small errors bars. Above the $PBLH_{MWR}$ the first lag correction presents higher differences in relation the other profiles at around 1350 m.

Figures 5-B and 5-C show the comparison of variance ($\sigma_{w\prime}^2$) and skewness ($S_{w\prime}$), respectively, with and without corrections. The profiles corrected by -2/3 law do not present significant differences in comparison to uncorrected profiles. On the other hand, the profiles corrected by the first lag correction have slight differences under the $PBLH_{MWR}$, mainly the $\sigma_{w\prime}^2$ ($S_{w\prime}$only in the first 50 m**).** Therefore, although the presence of ε can change slightly the value of high order moments, it is not enough to distort the observed phenomena as shown by the impact of the corrections applied.

For EL we use the same procedure for the correction and error analysis that we apply to the DL data. The same day was chosen (19th May), however the period selected is between 12 and 13 UTC, due to the incomplete overlap of Mulhacen.

In this sense, we studied the influence of noise at two wavelengths: 1064 nm, that has been previously analyzed by Pal et al. (2010) as presented in the section 2 and adopted as reference (considering the rather low impact of molecular signal and the two ways transmittance shown in 9) and 532 nm, just in order to check the feasibility of this wavelength for turbulence studies considering its spread use in observation network with higher reliability than 1064 nm. Figures 6 and 7 shows the autocovariance function, obtained from RCS'_{1064} and RCS'_{532}, respectively, at three distinct heights. As expected, in both cases the increase of height produces the increase of ε, principally above the $PBLH_{MWR}$. However, the wavelength 532 nm is more influenced by the noise, what can be verified by the higher peak at lag 0 in figure 7, in comparison with peaks at same lag in figure 6.

Figure 8-A shows the profiles corresponding to molecular backscatter coefficient, $\beta_{Molecular}$, and backscatter coefficient, β, at1064 nm ($\beta_{Molecular}^{1064}$ and $\beta_{Molecular}^{1064} + \beta_{Aerosol}^{1064}$, respectively),while figure 8-B

shows the same group of profiles at 532 nm ($\beta_{Molecular}^{532}$ and $\beta_{Molecular}^{532} + \beta_{Aerosol}^{532}$). It is evident the larger contribution of $\beta_{Aerosol}^{1064}$ to the total β at 1064 nm in comparion with the behavior at 532 nm, generating the higher values of noise at 532 nm in comparison with 1064 nm. This higher noise values are also due to higher extinction (by both aerosol and molecules) at 532 nm, producing a lower two-way transmittance. . As we used Elastic lidar technique, we could not calculate aerosol extinction profiles, but an estimation of these transmittances was done on the basis of Klett method (Klett, 1985). With this method, a constant lidar ratio value was constrained for each profile using the AOD derived from a collocated AERONET Sun-photometer [Guerrero-Rascado et al., 2008]. Using these constrained lidar ratios, the transmittances were calculated together with aerosol backscatter profiles, integrated up to 2.5 km. The estimated two-way transmittance was 0.85 for the case analyzed in this subsection (19th May).

Figures 9-A, 9-B, 9-C and 9-D show the vertical profiles of $\tau_{RCS'}$, $\sigma_{RCS'}^2$, $S_{RCS'}$ and kurtosis ($K_{RCS'}$), respectively, obtained at 1064 nm, with and without the corrections described in section 3.2. In general, the corrections do not affect the profiles generated from 1064 nm data in a significant way, so that, the higher influence of corrections is observed in the $K_{RCS'}$ profile, which is underestimated in some regions. In the figures 10-A, 10-B, 10-C and 10-D we show same high order moments calculated from 532 nm data. As the complexity of moments increases, it is possible to observe the larger influence of the corrections, due to propagation of noise. Nonetheless, the application of the corrections, mainly first lag correction, make these profiles very similar to those generated from the wavelength 1064 nm, so that the same phenomena can be observed in both.

Therefore, in spite of the larger attenuation expected at 532 nm wavelength that increases the noise of the profiles in comparison with 1064 nm, the application of the proposed corrections, mainly the first lag, reduces significantly the influence of noise and enable the observation of the same phenomena detected in the high-order moments obtained from 1064 nm. Consequently, the wavelength 532 nm will be applied in the analysis presented in section 4.2. Due to the first lag correction generates a higher impact on the without correction profiles, we adopted such correction in order to be more careful in the analyses of high-order moments obtained from DL and EL data.

4.2 Case studies

In this section we present two study cases, in order to show how the products indicated in table 2 can provide a detailed description about the turbulence in the PBL. The first case represents a typical day with a clear sky situation. The second case corresponds to a more complex situation, where there is presence of clouds and Saharan mineral dust layers.

4.2.1 Case study I: clear sky situation

In this case study we use measurements gathered with DL, MWR and pyranometer during 24 hours. The EL was operated under operator-supervised mode between 08:20 to 18:00 UTC.

Figure 11 (A) shows the integral time scale obtained from DL data ($\tau_{w\prime}$). The gray areas represents the region where $\tau_{w\prime}$ is lower than the acquisition time of DL and, therefore, for this region it is not possible to analyze the turbulent processes. However, the gray area is located almost entirely above the $PBLH_{MWR}$ (white stars). Thus, the DL acquisition time allows us to observe the turbulence throughout the whole PBL. The gray areas, as well as, the black lines (air temperature), have the same meaning in Figures 11-B and 11-C.

The $\sigma_{w\prime}^2$ has low values during the entire period when the $SBL$is present (Figure 11-B). Nevertheless, as air temperature begins to increase (around 07:00 UTC), the $\sigma_{w\prime}^2$increases together, as well as, the $PBLH_{MWR}$. The $\sigma_{w\prime}^2$ reaches its maximum values in the middle of the day, when we also observe the maximum values of air temperature and $PBLH_{MWR}$.. The combination of $\sigma_{w\prime}^2$ and $PBLH_{MWR}$ provides us a better comprehension about the $PBLH$ growth speed, so that, in the moments where high values of $\sigma_{w\prime}^2$ are observed, it means higher values of Turbulent Kinetic Energy (TKE), which favor the fast ascension of $PBLH$. In the same way, during the afternoon when the $\sigma_{w\prime}^2$ begins to decrease, the $PBLH$ growth speed its reduced until the moment where the CBL height is almost constant.

The skewness ofw' ($S_{w\prime}$) is shown in Figure 11-C. The $S_{w\prime}$ is directly associated with the direction of turbulent movements. Thus, positive values (red regions) correspond with a surface-heating-driven boundary layer, while negative (blue regions) ones are associated to cloud-top long-wave radiative cooling. During the stable period, there is predominance of low absolute values of $S_{w\prime}$. Nevertheless, as air temperature increases (transition from stable to unstable period), $S_{w\prime}$ values begin to become larger. Air temperature begins to decrease around 18:00 UTC, and there is a reduction of $S_{w\prime}$, so that, the generation rate of convective turbulence decreases. Therefore, the turbulence cannot be maintained against dissipation, then the CBL becomes a SBL covered by the RL. So, the reduction observed in the $PBLH_{MWR}$ is due to the $SBLH$ detection.

Figure 11-D shows the values of net surface radiation (R_n) that are estimated from solar global irradiance values using the seasonal model described in Alados et al. (2003). The negative values of R_n are concentrated in the stable region. The R_n begins to increase around 06:00 UTC and reaches its maximum in the middle of the day. Comparing figures 8-C and 8-D, we can observe similarity among the behavior of $S_{w\prime}$ and R_n, so that, the joint analysis of these variables reinforce the characterization of this PBL as surface-heating-driven CBL.

The increase of R_n causes the rise of surface air temperature, which contributes to the positive latent heat flux from the surface and, consequently, the growth of the $PBLH_{MWR}(CBL)$. TheR_n begins to decrease certain time before the air temperature and $S_{w\prime}$, but the intense reduction this variables, as well as, the detection of the $SBLH$ occur when R_n becomes negative again, although there can still be a positive sensible heat flux, what is characteristic of early evening in urban regions due to the release of the ground heat flux at that time.

Figure 11-E presents the values of surface air temperature and surface relative humidity (RH). Air surface temperature has a pattern of increase and decrease similar to observed in R_n and $S_{w\prime}$, as expected. On the

other hand, RH is inversely correlated with temperature and, thus, with the rest of variables, due to the relative constancy of the water vapor mixing ratio characteristic of our site during the study.

Figure 12 shows the RCS_{532} profile obtained from 08:00 to 18:00 UTC. At the beginning of the measurement period (08:20 to 10:00 UTC) it is possible to observe the presence of a thin residual layer (around 2000 m a.s.l.), and later from 13:00 to 18:00 UTC it is evident a lofted aerosol layer. In this picture there are the $PBLH_{MWR}$ (pink stars), the $PBLH_{Doppler}$ (blue stars), obtained from the maximum of σ_w^2, (Moreira et al., 2018a), and the $PBLH_{Elastic}$ (black stars), obtained from the maximum of σ_{RCS}^2, (Moreira et al., 2015). In the initial part of measurement, all profiles have similar behavior. However due to distinct $PBLH$ definition and tracer applied by each one, the differences increase as CBL becomes more complex, e.g. the presence of lofted aerosol layer at 14 UTC. The joint observation of the results provided by these three methods can provide us information about the sublayers in the PBL, both in convective and stable situations. Due to low variability of $PBLH$, the period between 13:00 and 14:00 UTC has been selected to be analyzed from the high order moments.

Figure 13 presents the statistical moments generated from RCS' of wavelength 532 nm, which were obtained from 13:00 and 14:00 UTC. The red line in all graphics represent the $PBLH_{Elastic}$ (2200 m a.s.l.) and the blue one the average value of $PBLH_{MWR}$ (2250 m a.s.l.), both obtained between 13 and 14 UTC.

Due to well-defined PBL, $PBLH_{Elastic}$ and $PBLH_{MWR}$ do not have significant differences (50 m). The σ_{RCS}^2, has small and practically constant values between 1000 and 1400m, evidencing the homogeneity of aerosol distribution in this region. From 1400 m the value of σ_{RCS}^2, begins to increase, reaching the maximum value at $PBLH_{Elastic}$, which represents the Entrainment Zone (region characterized by a intense mixing between air parcels coming fromCBL and FT, causing a high variation in aerosol concentration). Above $PBLH_{Elastic}$ the values of σ_{RCS}^2, decrease slowly due to location of the lofted aerosol around 2500 m. However, above this aerosol layer the value of σ_{RCS}^2, is reduced to zero, indicating a large homogeneity in aerosol distribution at this region, what is expected, because the aerosol concentration at the FT is negligible in this case. The integral time scale obtained from RCS' (τ_{RCS},) has values higher than EL time acquisition throughout the CBL, evidencing the feasibility for studying turbulence using this elastic lidar configuration. The skewness values obtained from RCS' (S_{RCS},) give us information about aerosol motion. The positive values of S_{RCS},observed in the lowest part of profile and above the $PBLH_{Elastic}$ represents the updrafts aerosol layers. The negative values of S_{RCS},indicates the region with low aerosol concentration due to clean air coming from free troposphere (FT)..This movement of ascension of aerosol layers and descent of clean air with zero value of S_{RCS},at $PBLH$ (characteristic of the CBL growing) was also detected by Pal et al. (2010) and McNicholas et al. (2014). The kurtosis of RCS' (K_{RCS},) determines the level of mixing at different heights. There are values of K_{RCS},larger than 3 in the lowest part of profile and around 2500 m, showing a peaked distribution in this region. On other hand, values of K_{RCS},lower than 3 are observed close to the $PBLH_{Elastic}$, therefore this region has a well-mixed CBL regime. Pal et al. (2010) and McNicholas et al. (2014) also detected this feature in the region nearby the $PBLH$. In figure 14 are shown the high-order moments obtained at the same period described above, however from the 1064 nm data (our reference wavelength). It is possible to observe a similarity between the profiles obtained from each wavelength, so that, the same

phenomena observed in the profiles generated from 532 nm and described above, also are detected in the profiles obtained from the reference wavelength.

The results provided by DL, pyranometer and MWR data agree with the results observed in Figure 10. In the same way, the analysis of high order moments of RCS' fully agree with the information in Figure 8. Thus, the large values of $S_{RCS'}$ and $K_{RCS'}$ detected around 2500 m a.s.l, where we can see a lofted aerosol layer, suggest the ascent of an aerosol layer and presence of a peaked distribution, respectively.

4.2.2 Case study: dusty and cloudy scenario

In this case study measurements with DL, MWR and pyranometer expand during 24 hours, while EL data are collected from 09:00 to 16:00 UTC.

Figure 15-A shows $\tau_{w'}$, where the black lines and gray area has the same meaning mentioned earlier. Outside the period 13:00 to 17:00 UTC, the grey area is situated completely above the $PBLH_{MWR}$ (white stars), thus DL time acquisition is enough to perform studies about turbulence in this case.

$\sigma_{w'}^2$ has values close to zero during all the stable period (Figure 15-B). However, when air temperature begins to increase (around 06:00 UTC), the $\sigma_{w'}^2$ also increases and reaches its maximum in the middle of the day. The higher values of PBL growth speed are observed in the moments where $\sigma_{w'}^2$ reaches its maximum values. In the late afternoon, as air temperature decrease, the values of $\sigma_{w'}^2$ (and consequently the TKE) decrease gradually, until reach the minimum value associated to the SBL. Figure 15-C shows the profiles of $S_{w'}$. The main features of this case are: the low values of $S_{w'}$, the slow increase and ascension of positive $S_{w'}$ values and the predominance of negative $S_{w'}$ values from 12:00 to 13:00 UTC. The first two features are likely due to the presence of the intense Saharan dust layer (Figure 16), which reduces the transmission of solar irradiance, and consequently the absorption of solar irradiance at the surface, generating weak convective process. From Figure 15 we can observe the presence of clouds from 12:00 to 14:00 UTC. This justifies the intense negative values of $S_{w'}$ observed in this period, because, as mentioned before, $S_{w'}$ is directly associated with direction of turbulent movements that during this period is associated to cloud-top long-wave radiative cooling, due to the presence of clouds (Ansmann et al., 2010).

The influence of Saharan dust layer can also be evidenced on the R_n pattern (Figure 15-D), which maintains negative values until 12:00 UTC and reaches a low maximum value (around 200 W/m²). The observation of $S_{w'}$ and R_n between 12:00 and 14:00 reinforce the idea of a case of the cloud-top long-wave radiative cooling in the CBL. Air surface temperature and RH (Figure 14-E) present the same correlation and anti-correlation (respectively) observed in the earlier case study, where the maximum of air surface temperature and the minimum of RH are detected in coincidence with the maximum daily value of $PBLH_{MWR}$.

As mentioned before, Figure 16 shows the RCS profile obtained from 09:00 to 16:00 UTC in a complex situation, with presence of decoupled dust layer (around 3800 m a.s.l.) from 09:00 to 12:00 UTC and clouds (around 3500 m a.s.l.) from 11:00 to 16:00 UTC. The pink, black and blue stars represent the $PBLH_{MWR}$, $PBLH_{Doppler}$ and $PBLH_{Elastic}$ respectively. Due to the presence of dusty layers and clouds, the difference

between the methods is more evident, mainly of the $PBLH_{Elastic}$, which uses the aerosol as tracers. This method only produces results close to the others at 15 UTC, when dust layer is mixed with the CBL.

Figure 17 illustrates the statistical moments of RCS' of 532 nm wavelength obtained from 11:00 to 12:00 UTC. The σ^2_{RCS}, profile presents several peaks due to the presence of distinct aerosol sublayers. The first peak is coincident with the value of $PBLH_{MWR}$. The value of $PBLH_{elastic}$, is coincident with the base of the dust layer. This difficulty to detect the $PBLH$ in presence of several aerosol layers is inherent to the variance method (Kovalev and Eichinger, 2004). However, the joint observation of $PBLH_{MWR}$ and $PBLH_{elastic}$, enable us to characterize and distinguish the several sublayers. The values of τ_{RCS},are higher than EL acquisition time all along the PBL, evidencing the feasibility of EL time acquisition for studying the turbulence of PBL in this case. The S_{RCS},profile has several positive values, due to the large number of aerosol sublayers that are present. The characteristic inflection point of S_{RCS},is observed in coincidence with the $PBLH_{MWR}$, that confirming the agreement between this point and the $PBLH$. From the analysis of S_{RCS}, and S_w,is possible to justify this phenomena from the mixing process demonstrated in the earlier case study. The K_{RCS},has predominantly values lower than 3 below 2500 m, thus shown how this region is well mixed as can see in Figure 16. Values of K_{RCS},larger than 3 are observed in the highest part of profile, where the dust layer is located.

In order to show the feasibility of 532 nm wavelength, in the figure 18 are presented the high-order moments obtained between 11-12 UTC from 1064 nm wavelength data. Although the error of σ^2_{RCS}, obtained from 532 nm (pink shadow) is considerably higher than the error of same variable obtained from 1064 nm, all profiles are very similar, so that, the same phenomena can be observed in both graphics (figure 17 and 18).

Figure 19 shows the RCS' 532 nm wavelength high-order moments obtained from 12:00 and 13:00 in presence of cloud cover. The method based on maximum of σ^2_{RCS},locates the $PBLH_{Elastic}$ at the cloud base, due to the high variance of RCS' generated by the clouds. τ_{RCS}, presents values larger than EL time acquisition, therefore this configuration enable us to study turbulence by EL analyses. S_{RCS}, has few peaks, due to the mixing between CBL and dust layer, generating a more homogenous layer. The highest values of S_{RCS},are observed in regions where there are clouds, and the negative ones (between 3500 and 4000 m) occur due to presence of air from FT between the two aerosol layers (Figure 16). The inflection point of S_{RCS},profile is observed in $PBLH_{MWR}$ region. K_{RCS},profile has low values in most of the PBL, demonstrating the high level of mixing during this period, where dust layer and PBL are combined. The higher values of K_{RCS},are observed in the region of clouds. In the same way of the previous analysis, the high-order moments of the period mentioned above were calculated for the wavelength of 1064 nm (figure 20). Although there are some differences in the absolute values of some profiles, the high-order moments generated using 1064 and 532 nm have similar profiles, so that, the same phenomena can be observed, demonstrating the viability of 532 nm wavelength in the proposed methodology.

5 Conclusions

In this paper we perform an analysis about the PBL turbulent features from three different types of remote sensing systems (DL, $EL$and MWR) and surface sensors during SLOPE-I campaign. We applied two kind of corrections to the lidar data: first lag and -2/3 corrections. The corrected DL statistical moments showed little variation with respect to the uncorrected profiles, denoting a rather low influence of the noise. The EL high-order moments were obtained from two wavelengths: 1064 nm, adopted as reference, and 532 nm, in order to verify the viability to use the last one in turbulence analysis. From this comparison, was possible to observe that the wavelength 532 nm is more affected by noise, in comparison with 1064 nm, due to the large contribution of the molecular component and the lower two ways transmittance at that wavelength. However, the application of proposed corrections, mainly the first lag, can reduce such influence, so that, the same phenomena can be observed in the high-order moments provided from both wavelengths

The case studies present two kind of situations: well-defined PBL and a more complex situation with the presence of Saharan dust layer and some clouds. In both cases was possible to identify the events describe in table 2. The combined use of remote sensing systems shows how the results provided by the different instruments can complement one each other, providing a detailed observation of some phenomena, mainly in complex situations.

Therefore, this study shows the feasibility of the described methodology based on the combination of remote sensing systems for retrieving a detailed picture on the PBL turbulent features. In addition, the feasibility of using the analyses of high order moments of the RCS collected at 532 nm at a temporal resolution of 2 s offers the possibility for using the proposed methodology in networks such as EARLINET or LALINET with a reasonable additional effort.

Acknowledgements

This work was supported by the Andalusia Regional Government through project P12-RNM-2409, by the Spanish AgenciaEstatal de Investigación, AEI, through projects CGL2016-81092-R and CGL2017-90884-REDT. We acknowledge the financial support by the European Union's Horizon 2020 research and innovation program through project ACTRIS-2 (grant agreement No 654109). The authors thankfully acknowledge the FEDER program for the instrumentation used in this work and the University of Granada that supported this study through the Excellence Units Program and "Plan Propio. Programa 9 Convocatoria 2013".

References

Alados, I., Foyo-Moreno, I., Olmo, F. J., Alados-Arboledas, L. Relationship between net radiation and solar radiation for semi-arid shrub-land. Agr. Forest Meteorol., 116, 221-227, 2003.

Albrecht, B. A., Bretherton, C. S., Johnson, D., Scubert, W. H., and Frisch, A. S.: The Atlantic stratocumulus transition experiment—ASTEX, Bull. Am. Meteorol. Soc., 76, 889–904, 1995.

493 Andrews, E., Sheridan, P. J. ,Ogren, J. A., and Ferrare, R.: In situ aerosol profiles over the Southern Great
494 Plains cloud and radiation test bed site: 1. Aerosol optical properties, J. Geophys. Res., 109, D06208,
495 doi:10.1029/2003JD004025, 2004.

496 Ansmann, A., Fruntke, J., Engelmann, R. Updraft and downdraft characterization with Doppler lidar: cloud-
497 free versus cumuli-topped mixed layer. Atmos. Chem. Phys., 10, 7845-7858, 2010.

498 Antón, M., Valenzuela, A., Cazorla, A., Gil, J. E., Gálvez-Fernández, J., Lyamani, H., Foyo-Moreno, I.,
499 Olmo, F. J., Alados-Arboledas, L. Global and diffuse shortwave irradiance during a strong desert dust
500 episode at Granada (Spain). Atmos. Res., 118, 232 – 239, 2012.

501 Bedoya-Velásquez, A. E., Navas-Guzmán, F., Granados-Muñoz, M. J., Titos, G., Román, R., Casquero-
502 Vera, J. A., Ortiz-Amezcua, P., Benavent-Oltra, J. A., Moreira, G. de A., Montilla-Rosero, E., Ortiz, C. D.
503 H., Artiñano, Coz, E., Alados-Arboledas, L., Guerrero-Rascado, J. L. Hygroscopic growth study in the
504 framework of EARLINET during the SLOPE I campaign: synergy of remote sensing and in-situ
505 instrumentation. Atmos. Chem. Phys., 18, 7001-7017, 2017.

506 Behrendt, A., Wulfmeyer, V., Hammann, E., Muppa, S. K., Pal, S.: Profiles of second- to
507 fourth-order moments of turbulent temperature fluctuations in the convective boundary layer : first
508 measurements with rotational Raman lidar. Atmos. Chem. Phys., 15, 5485–5500.
509 https://doi.org/10.5194/acp-15-5485-2015, 2015.

510 Bravo-Aranda, J. A., Navas-Guzmán, F., Guerrero-Rascado, J. L., Pérez-Ramírez, D., Granados-Muñoz,
511 M. J., Alados-Arboledas, L. Analysis of lidar depolarization calibration procedure and application to the
512 atmospheric aerosol characterization. Int. J. Remote Sens., 34 (9-10), pp. 3543-3560, 2013.

513 Caumont, O., Cimini, D., Löhnert, U., Alados-Arboledas, L., Bleisch, R., Buffa, F., Ferrario, M.E., Haefele,
514 A., Huet, T., Madonna, F., Pace, G. Assimilation of humidity and temperature observations retrieved from
515 ground-based microwave radiometers into a convective-scale NWP model. Q. J. Roy. Meteor. Soc., 142
516 (700), pp. 2692-2704, 2016.

517 Engelmann, R.; Wandinger, U.; Ansmann, A.; Müller, D.; Žeromskis, E.;
518 Althausen, D.; Wehner, B. Lidar Observations of the Vertical Aerosol Flux in the Planetary
519 Boundary Layer. J. Atmos. Ocean. Tech., v. 25, n. 8, p. 1296–1306, 2008.

520 Guerrero-Rascado, J.L., Ruiz, B., Alados-Arboledas, L. Multi-spectral lidar characterization of the vertical
521 structure of Saharan dust aerosol over Southern Spain. Atmos. Environ., 42, 2668-2681, 2008.

522 Guerrero-Rascado, J.L., Olmo, F.J., Avilés-Rodríguez, I., Navas-Guzmán, F., Pérez-Ramírez, D., Lyamani,
523 H., Alados-Arboledas, L.: Extreme Saharan dust event over the southern Iberian Peninsula in September
524 2007: Active and passive remote sensing from surface and satellite. Atmos. Chem. Phys., 9, 21, 8453-8469,
525 2009.

526 Guerrero-Rascado, J. L., Costa, M. J., Bortoli, D., Silva, A. M., Lyamani, H., Alados-Arboledas, L. Infrared
527 lidar overlap function: an experimental determination, Opt. Express, 18, 20350-20359, 2010

Guerrero-Rascado, J. L., Landulfo, E., Antuña, J. C., Barbosa, H. M. J., Barja, B., Bastidas, A. E., Bedoya, A. E., da Costa, R. F., Estevan, R., Forno, R. N., Gouveia, D. A., Jimenez, C., Larroza, E. G., Lopes, F. J. S., Montilla-Rosero, E., Moreira, G. A., Nakaema, W. M., Nisperuza, D., Alegria, D., Múnera, M., Otero, L., Papandrea, S., Pawelko, E., Quel, E. J., Ristori, P., Rodrigues, P. F., Salvador, J., Sánchez, M. F., and Silva, A.: Latin American Lidar Network (LALINET) for aerosol research: diagnosis on network instrumentation, J. Atmos. Sol.-Terr. Phy., 138–139, 112–120, 2016.

Illingworth, A. J., Hogan, R. J. O' Connor, E. J. Bouniol, D. Brooks, M. E. Delanoe, J. Donovan, D. P. Eastment, J. D. Gaussiat, N. Goddard, J. W. F. Haeffelin, M. Klein Baltink, H. Krasnov, O. A. Pelon, J. Piriou, J.-M. Protat, A. Russchenberg, H. W. J. Seifert, A. Tompkins, A. M. Van Zadelhoff, G.-J. Vinit, F. Willen, U. Wilson, D. R. and Wrench, C . L.: CLOUDNET: Continuous Evaluation of Cloud Profiles in Seven Operational Models using Ground-Based Observations. Bull. Am. Meteorol. Soc., 88, 883-898, doi:10.1175/BAMS-88-6-883, 2007.

Kaimal, J. C., and Gaynor, J. E.: The Boulder Atmospheric Observatory, J. Clim. Appl. Meteorol., 22, 863–880, 1983.

Kiemle, C., Brewer, W. A., Ehret, G., Hardesty, R. M., Fix, A., Senff, C., Wirth, M., Poberaj, G., and LeMone, M. A.: Latent heat flux profiles from collocated airborne water vapor and wind lidars during IHOP 2002, J. Atmos. Ocean. Tech., 24, 627–639, 2007.

Klett, J. D.: Lidar inversion with variable backscatter/extinction ratios, Appl. Opt., 24, 1638-1643, https://doi.org/10.1364/AO.24.001638, 1985.

Kovalev, V.A., Eichinger, W.E., Elastic Lidar, Wiley 2004.

Lenschow, D. H., Wyngaard, J. C., and Pennell, W. T.: Mean-field and second-moment budgets in a baroclinic convective boundary layer, J. Atmos. Sci., 37, 1313–1326, 1980.

Lenschow, D. H., Mann, J., and Kristensen, L.: How long is long enough when measuring fluxes and other turbulence statistics?, J. Atmos. Oceanic Technol., 11, 661–673, 1994.

Lenschow, D. H., Wulfmeyer, V. and Senff, C.: Measuring second- through fourth-order moments in noisy data, J. Atmos. Oceanic Technol., 17, 1330–1347, 2000.

Lenschow, D. H., Lothon, M., Mayor, S. D., Sullivan, P. P., and Canut, G.: A comparison of higher-order vertical velocity moments in the convective boundary layer from lidar with in situ measurements and large-eddy simulation, Bound-Lay. Meteorol., 143, 107–123, doi:10.1007/s10546-011-9615-3., 2012.

Lothon, M., Lenschow, D. H., and Mayor, S. D.: Coherence and scale of vertical velocity in the convective boundary layer from a Doppler lidar, Bound.-Lay. Meteorol., 121, 521–536, 2006.

Lyamani, H., Olmo, F. J., Alcántara, A., and Alados-Arboledas, L.: Atmospheric aerosols during the 2003 heat wave in southeastern Spain I: Spectral optical depth, Atmos. Environ., 40, 6453–6464, 2006

McNicholas, C., Turner, D. D. Characterizing the convective boundary layer turbulence with a High Spectral Resolution Lidar. J. Geophys Res-Atmos., v. 119, p. 910–927, 2014.

Muppa, K.S., Behrendt, A., Späth, F., Wulfmeyer, V., Metzendorf, S., Riede, A.: Turbulent humidity fluctuations in the convective boundary layer: Cases studies using water vapour differential absorption lidar measurements. Bound-Lay. Meteorol., 158, 43-66, DOI 10.1007/s10546-015-0078-9, 2014.

Monin, A. S., Yaglom, A. M. Statistical Fluid Mechanics, Vol. 2. MIT Press, 874 pp, 1979.

Moreira, G. de A., Marques, M. T. A., Nakaema, W., Moreira, A. C. de C. A., Landulfo, E. Planetary boundary height estimations from Doppler wind lidar measurements, radiosonde and hysplit model comparisom. Óptica Pura y Aplicada, 48, 179-183, 2015

Moreira, G. de A., Guerrero-Rascado, J. L., Bravo-Aranda, J. A., Benavent-Oltra, Ortiz-Amezcua, P., Róman, R., Bedoya-Velásquez, A., Landulfo, E., Alados-Arboledas, L. Study of the planetary boundary layer by microwave radiometer, elastic lidar and Doppler lidar estimations in Southern Iberian Peninsula. Atmos. Res., 213, 185-195, 2018a.

Moreira, G. de A., Lopes, F. J. S., Guerrero-Rascado, J. L., Landulfo, E., Alados-Arboledas, L. Analyzing turbulence in Planetary Boundary Layer from multiwavelenght lidar system: impact of wavelength choice. Opt. Express. Under review, 2018b.

Navas Guzmán, F., Guerrero Rascado, J. L., and Alados Arboledas, L.: Retrieval of the lidar overlap function using Raman signals, Óptica Pura y Aplicada, 44, 71–75, 2011.

Navas-Guzmán, F., Bravo-Aranda, J.A., Guerrero-Rascado, J.L, Granados-Muñoz, M.J, and Alados-Arboledas, L.: Statistical analysis of aerosol optical properties retrieved by Raman lidar over Southeastern Spain. Tellus B, 65, 21234, 2013.

Navas-Guzmán, F., Fernández-Gálvez, J., Granados-Muñoz, M.J, Guerrero-Rascado, J.L., Bravo-Aranda, J.A., and Alados-Arboledas, L.: Tropospheric water vapor and relative humidity profiles from lidar and microwave radiometry. Atmos. Meas. Tech., 7, 1201-1211, 2104.

O'Connor, E. J., Illingworth, A. J., Brooks, I. M., Westbrook, C. D., Hogan, R. J., Davies, F., Brooks, B. J.: A method for estimating the turbulent kinetic energy dissipation rate from a vertically-pointing Doppler lidar, and independent evaluation from balloon-borne in-situ measurements. J. Atmos. Ocean. Tech., v. 27, n. 10, 1652-1664, 2010.

Ortiz-Amezcua, P., Guerrero-Rascado, J.L., Granados-Muñoz, M.J., Bravo-Aranda, J. A., Alados-Arboledas, L. Characterization of atmospheric aerosols for a long range transport of biomass burning particles from canadian forest fires over the southern iberian peninsula in july 2013. Optica Pura y Aplicada, 47 (1), pp. 43-49, 2014.

Ortiz-Amezcua, P., Luis Guerrero-Rascado, J., Granados-Munõz, M.J., Benavent-Oltra, J.A., Böckmann, C., Samaras, S., Stachlewska, I.S., Janicka, L., Baars, H., Bohlmann, S., Alados-Arboledas, L. Microphysical characterization of long-range transported biomass burning particles from North America at three EARLINET stations. Atmos. Chem. Phys., 17 (9), pp. 5931-5946, 2017.

Pal, S.; Behrendt, a.; Wulfmeyer, V. Elastic-backscatter-lidar-based characterization of the convective boundary layer and investigation of related statistics. Ann. Geophys., v. 28, n. 3, p. 825–847, 2010.

Pappalardo, G., Amodeo, A., Apituley, A., Comeron, A., Freudenthaler, V., Linné, H., Ansmann, A., Bösenberg, J., D'Amico, G., Mattis, I., Mona, L., Wandinger, U., Amiridis, V., Alados-Arboledas, L., Nicolae, D., and Wiegner, M.: EARLINET: towards an advanced sustainable European aerosol lidar network. Atmos. Meas. Tech., 7, 2389-2409, doi:10.5194/amt-7-2389-2014, 2014.

Román, R., Benavent-Oltra, J. A., Casquero-Vera, J. A., Lopatin, A., Cazorla, A., Lyamani, H., Denjean, C., Fuertes, D., Pérez-Ramirez, D., Torres, B., Toledano, C., Dubovik, O., Cachorro, V. E., Frutos, A. M., Olmo, F. J., Alados-Arboledas, L. Retrieval of aerosol profiles combining sunphotometer and ceilometer measurements in GRASP code. Atmos. Res., 204, 161, 177, 2018.

Rose, T., Creewll, S., Löhnert, U., Simmer, C.: A network suitable microwave radiometer for operational monitoring of cloudy atmosphere. Atmos. Res., 75, 3, 183 – 200, 2005.

Stull, R. B., Santoso, E., Berg, L., Hacker, J.: Boundary layer experiment 1996 (BLX96), Bull. Am. Meteorol. Soc., 78, 1149–1158, 1997.

Stull, R. B.: An Introduction to Boundary Layer Meteorology, vol. 13, *Kluwer Academic Publishers, the Netherlands*, Dordrecht/Boston/London, 1988.

Stull, R. B.: Meteorology for Scientists and Engineers, 3rd Edition, *Uni. Of British Columbia*, 2011.

Titos, G., Foyo-Moreno, I., Lyamani, H., Querol, X., Alastuey, A., and Alados-Arboledas, L.: Optical properties and chemical composition of aerosol particles at an urban location: An estimation of the aerosol mass scattering and absorption efficiencies, J. Geophys.Res.-Atmos., 117, D04206, doi:10.1029/2011JD016671, 2012.

Turner, D. D., Ferrare, R. A., Wulfmeyer, V., and Scarino, A. J.: Aircraft evaluation of ground-based Raman lidar water vapor turbulence profiles in convective mixed layers, J. Atmos. Oceanic Technol., 31, 1078–1088, doi:10.1175/JTECH-D-13-00075-1, 2014

vanUlden, A. P., and Wieringa, J. :Atmospheric boundary layer research at Cabauw, Bound-Lay. Meteorol., 78,39–69, 1996.

Valenzuela, A., Olmo, F.J.ab, Lyamani, H.ab, Granados-Muñoz, M.J.ab, Antón, M.c, Guerrero-Rascado, J.L.ab, Quirantes, A.a, Toledano, C.d, Perez-Ramírez, D.ef, Alados-Arboledas, L.: Aerosol transport over the western mediterranean basin: Evidence of the contribution of fine particles to desert dust plumes over alborán island. J. Geophys Res., 119, 24, 14,028-14,044, 2014.

Vogelmann, A. M., McFarquhar, G. M., Ogren, J. A., Turner, D. D., Comstock, J. M., Feingold, G., Long, C. N., Jonsson, H. H., Bucholtz, A., Collins, D. R., Diskin, G. S., Gerber, H., Lawson, R. P., Woods, R. K., Andrews, E., Yang, H., Chiu, J. C., Hartsock, D., Hubbe, J. M., Lo, C., Marshak, A., Monroe, J. W.,

Mcfarlane, S. A., Jason, M., and Toto, T.: RACORO extended-term aircraft observations of boundary layer clouds, Bull. Am. Meteorol. Soc., 93, 861–878, doi:10.1175/BAMS-D-11-00189.1, 2012.

Williams, A. G., and Hacker, J. M.: The composite shape and structure of coherent eddies in the convective boundary layer, Bound-Lay. Meteorol., 61, 213–245, 1992.

Wulfmeyer, V.: Investigation of turbulent processes in the lower troposphere with water vapor DIAL and radar-RASS, J. Appl. Sci., 56, 1055–1076, 1999.

Wulfmeyer, V., Pal., S., Turner, D. D., and Wagner, E.: Can water vapour Raman lidar resolve profiles of turbulent variables in the convective boundary layer?, Bound-Lay. Meteorol., 136, 253–284, doi:10.1007/s10546-010-9494-z, 2010.

662 Table 1 – Variables applied to statistical analysis (Lenschow et al., 2000)

	Without Correction	Correction	Error
Integral Time Scale (τ)	$\int_0^{\infty} q'(t)dt$	$\frac{1}{\overline{q'^2}} \int_{t\to 0}^{\infty} M_{11}(t)dt$	$\tau . \sqrt{\frac{4\Delta M_{11}}{M_{11}(\to 0)}}$
Variance ($\sigma^2_{q'}$)	$\frac{1}{T}\sum_{t=1}^{T}(q(t) - \overline{q})^2$	$M_{11}(\to 0)$	$q^2 . \sqrt{\frac{4\Delta M_{11}}{M_{11}(\to 0)}}$
Skewness (S)	$\frac{\overline{q^3}}{\sigma_q^3}$	$\frac{M_{21}(\to 0)}{M_{11}^{3/2}(\to 0)}$	$\frac{\Delta M_{21}}{\Delta M_{11}^{3/2}}$
Kurtosis (K)	$\frac{\overline{q^4}}{\sigma_q^4}$	$\frac{3M_{22}(\to 0) - 2M_{31}(\to 0) - 3\Delta M_{11}^2}{M_{11}^2(\to 0)}$	$\frac{4\Delta M_{31} - 3\Delta M_{22} - \Delta M_{11}^2}{\Delta M_{11}^2}$

663

664

665

666 Table 2 – Products and their respective meaning, provided by each system

Product	System	Meaning
$\tau_{w'}(z)$	Doppler lidar	Measurement in time of length of turbulent eddies
$\sigma^2_{w'}(z)$	Doppler lidar	Turbulent Kinetic Energy
$S_{w'}(z)$	Doppler lidar	Direction of turbulent movements
$PBLH_{Doppler}$	Doppler lidar	Top of CBL obtained from variance threshold method
$\tau_{RCS'}(z)$	Elastic lidar	Measurement in time of length of turbulent eddies
$\sigma^2_{RCS'}(z)$	Elastic lidar	Homogeneity of aerosol distribution
$S_{RCS'}(z)$	Elastic lidar	Aerosol motion (S < 0 ➔ Downdrafts, S> 0➔ Updrafts)
$K_{RCS'}(z)$	Elastic lidar	Level of aerosol mixing (K < 3 ➔ Well-Mixed, K > 3 ➔ Low Mixing)
$PBLH_{Elastic}$	Elastic lidar	Top of aerosol layer obtained from variance method
$PBLH_{MWR}$	MWR	Top of CBL/SBL layer obtained from Potential Temperature

667

668

669

670

671

672

673

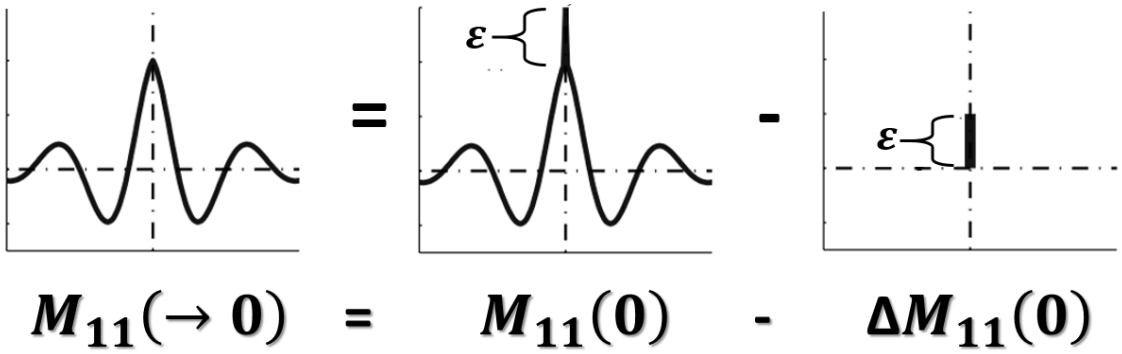

Figure 1 – Procedure to remove the errors of autocovariance functions. $M_{11}(\rightarrow 0)$ – corrected autocovariance function errors; $M_{11}(0)$ - autocovariance function without correction; $\Delta M_{11}(0)$ - error of autocovariance function.

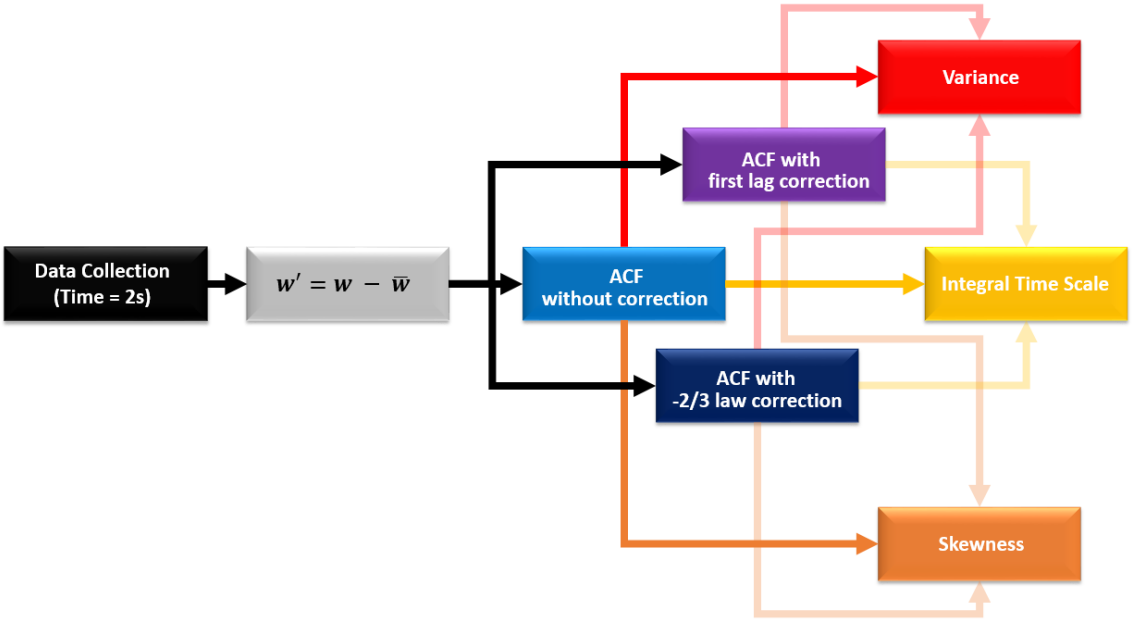

Figure 2 – Flowchart of data analysis methodology applied to the study of turbulence with Doppler lidar

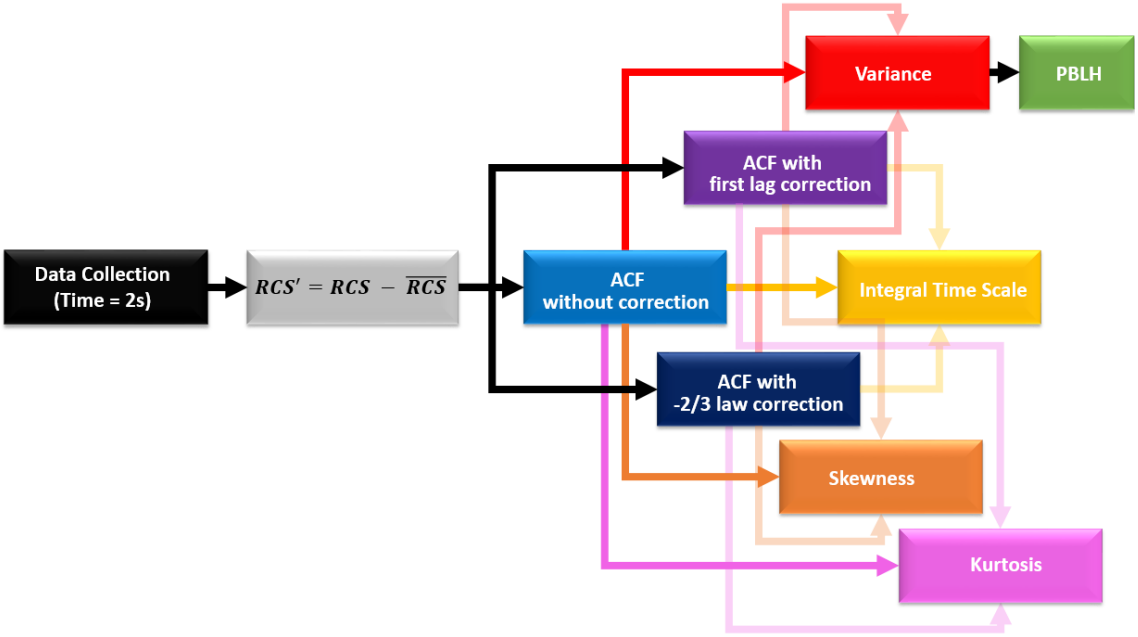

Figure 3 – Flowchart of data analysis methodology applied to the study of turbulence with elastic lidar

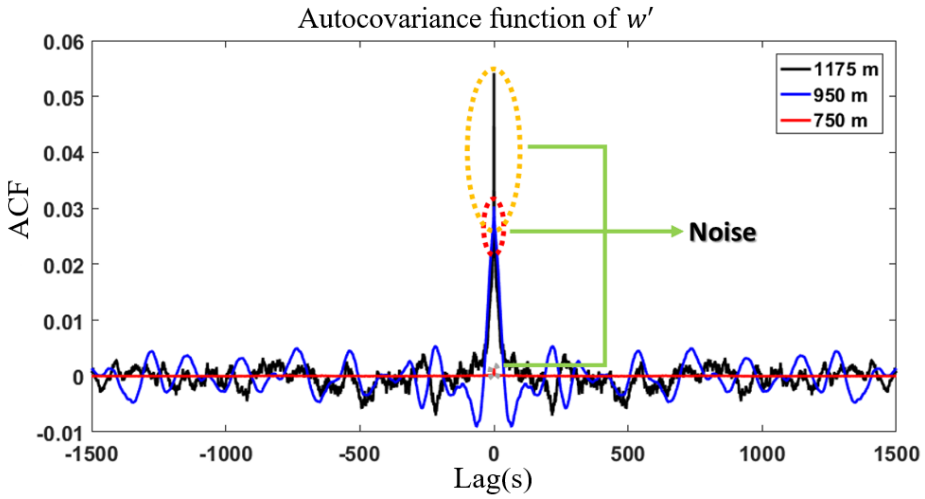

Figure 4 – Autocovariance function (ACF) of w', obtained from Doppler lidar at three different heights on 19th May 2016 at 08-09 UTC in Granada.

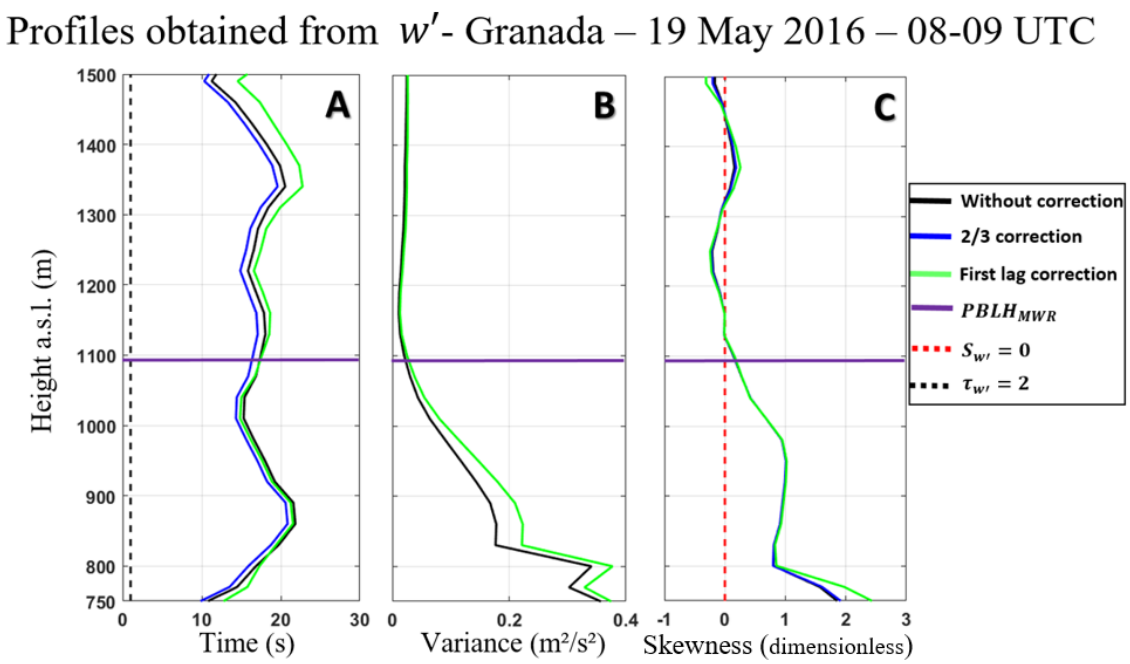

Figure 5 – A - Vertical profile of Integral time scale ($\boldsymbol{\tau_{w'}}$). B - Vertical profile of variance ($\boldsymbol{\sigma^2_{w'}}$). C - Vertical profile of Skewness ($\boldsymbol{S_{w'}}$). All profiles were obtained from Doppler lidar data on 19th May 2016 at 08-09 UTC in Granada.

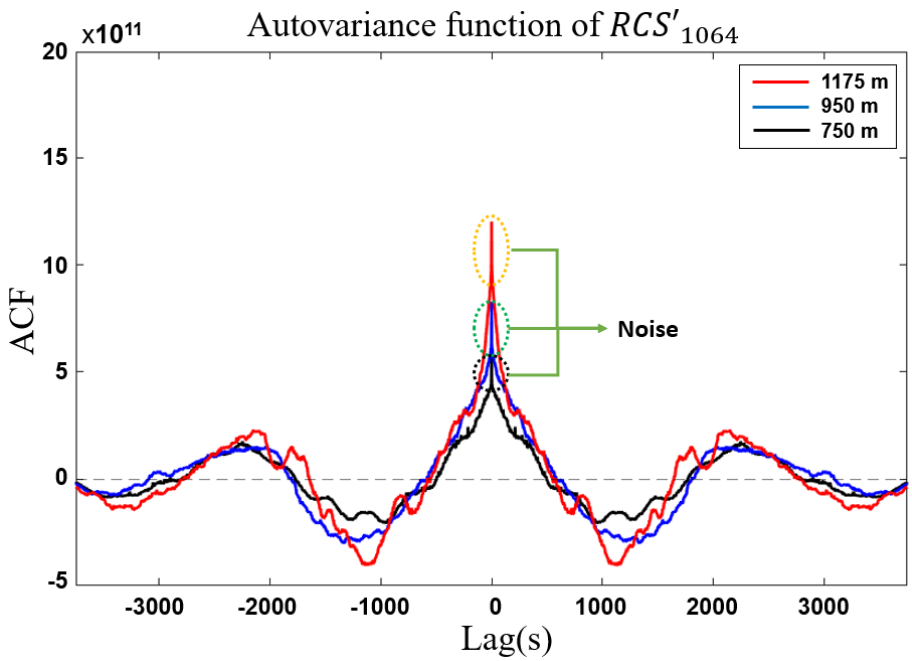

Figure 6 – Autocovariance of $\boldsymbol{RCS'_{1064}}$ obtained from Mulhacen elastic lidar data to three different heights on 19th May 2016 at 12-13 UTC in Granada.

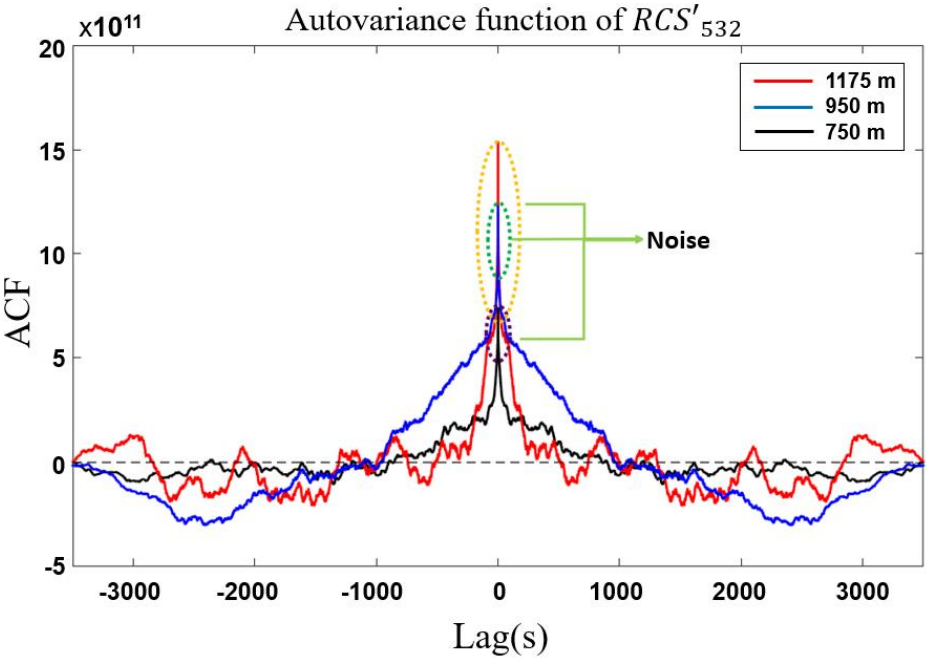

Figure 7 – Autocovariance of $\boldsymbol{RCS'_{532}}$ obtained from Mulhacen elastic lidar data to three different heights on 19th May 2016 at 12-13 UTC in Granada.

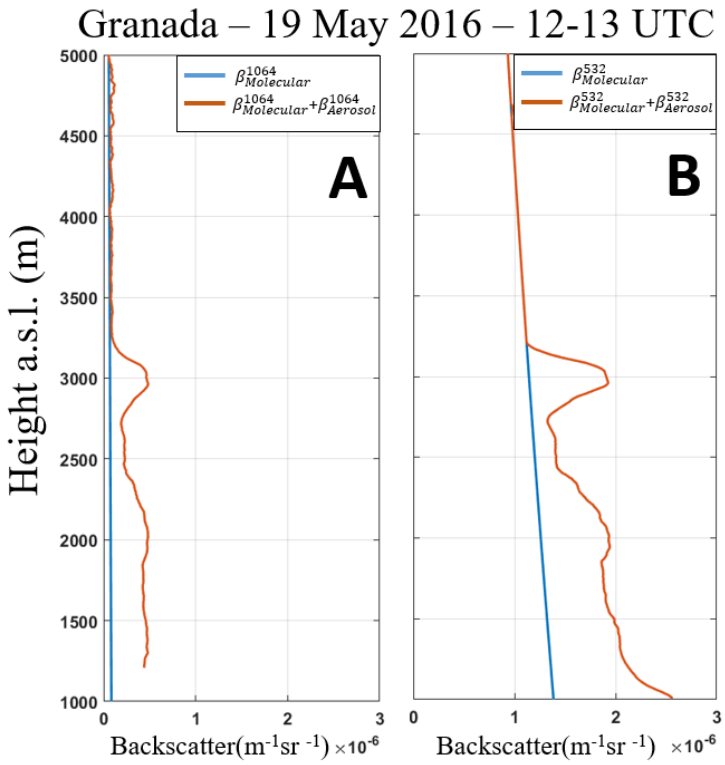

Figure 8 – (A) $\beta^{1064}_{Molecular}$ (blue line) and $\beta^{1064}_{Molecular} + \beta^{1064}_{Aerosol}$ (orange line). (B) $\beta^{532}_{Molecular}$ (blue line) and $\beta^{532}_{Molecular} + \beta^{532}_{Aerosol}$ (orange line). All profiles were obtained from Mulhacen elastic lidar data on 19th May 2016 between 12-13 UTC in Granada.

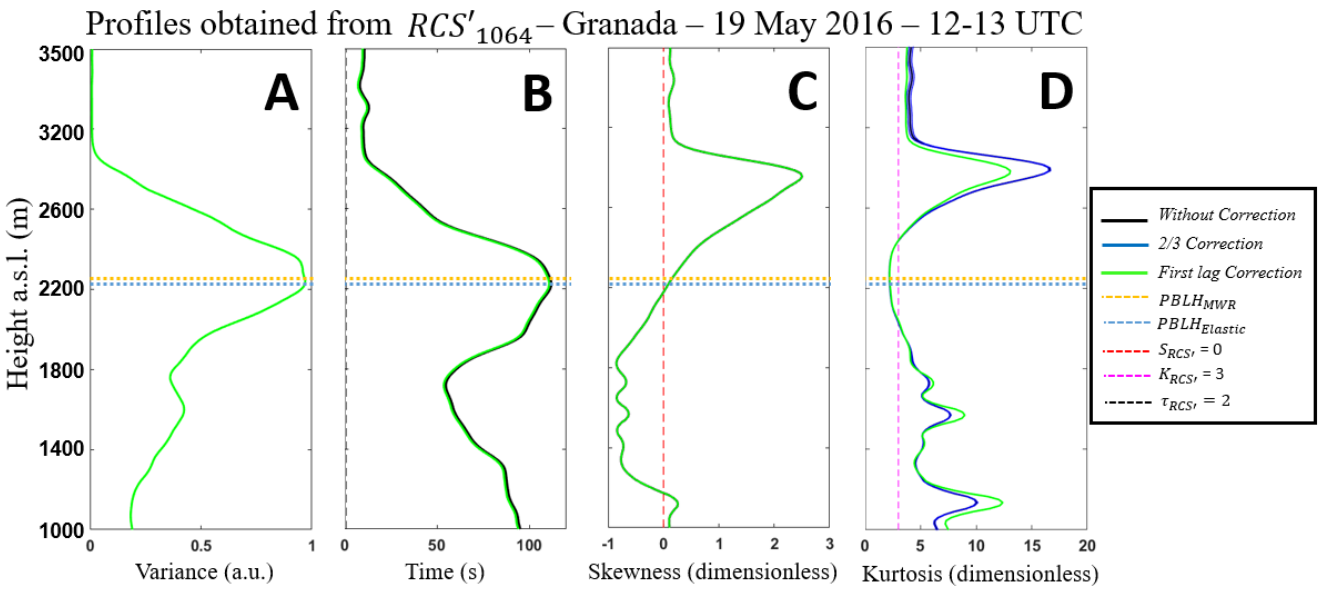

Figure 9 – A- Vertical profile of Integral time scale ($\boldsymbol{\tau_{RCS'}}$). B - Vertical profile of variance ($\boldsymbol{\sigma^2_{RCS'}}$). C - Vertical profile of Skewness ($\boldsymbol{S_{RCS'}}$). D - Vertical profile of Kurtosis ($\boldsymbol{K_{RCS'}}$). All profiles were obtained from Mulhacen elastic lidar data on 19th May2016 in Granada between 12-13 UTC.

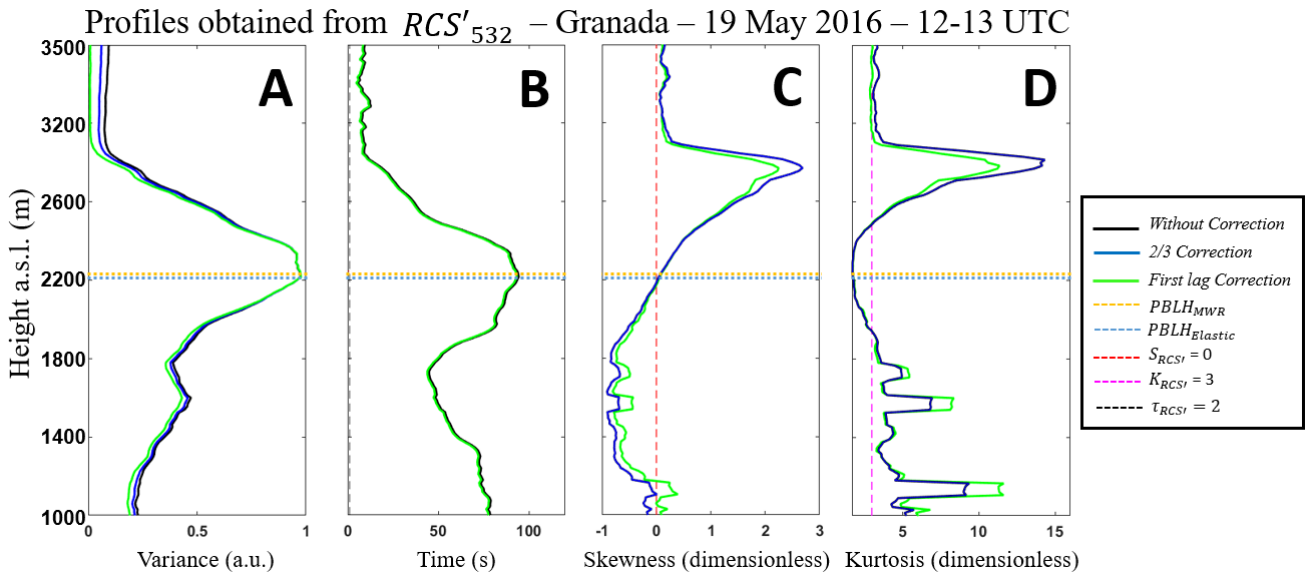

Figure 10 – A- Vertical profile of Integral time scale ($\boldsymbol{\tau_{RCS'}}$). B - Vertical profile of variance ($\boldsymbol{\sigma^2_{RCS'}}$). C - Vertical profile of Skewness ($\boldsymbol{S_{RCS'}}$). D - Vertical profile of Kurtosis ($\boldsymbol{K_{RCS'}}$). All profiles were obtained from Mulhacen elastic lidar data on 19th May2016 in Granada between 12-13 UTC.

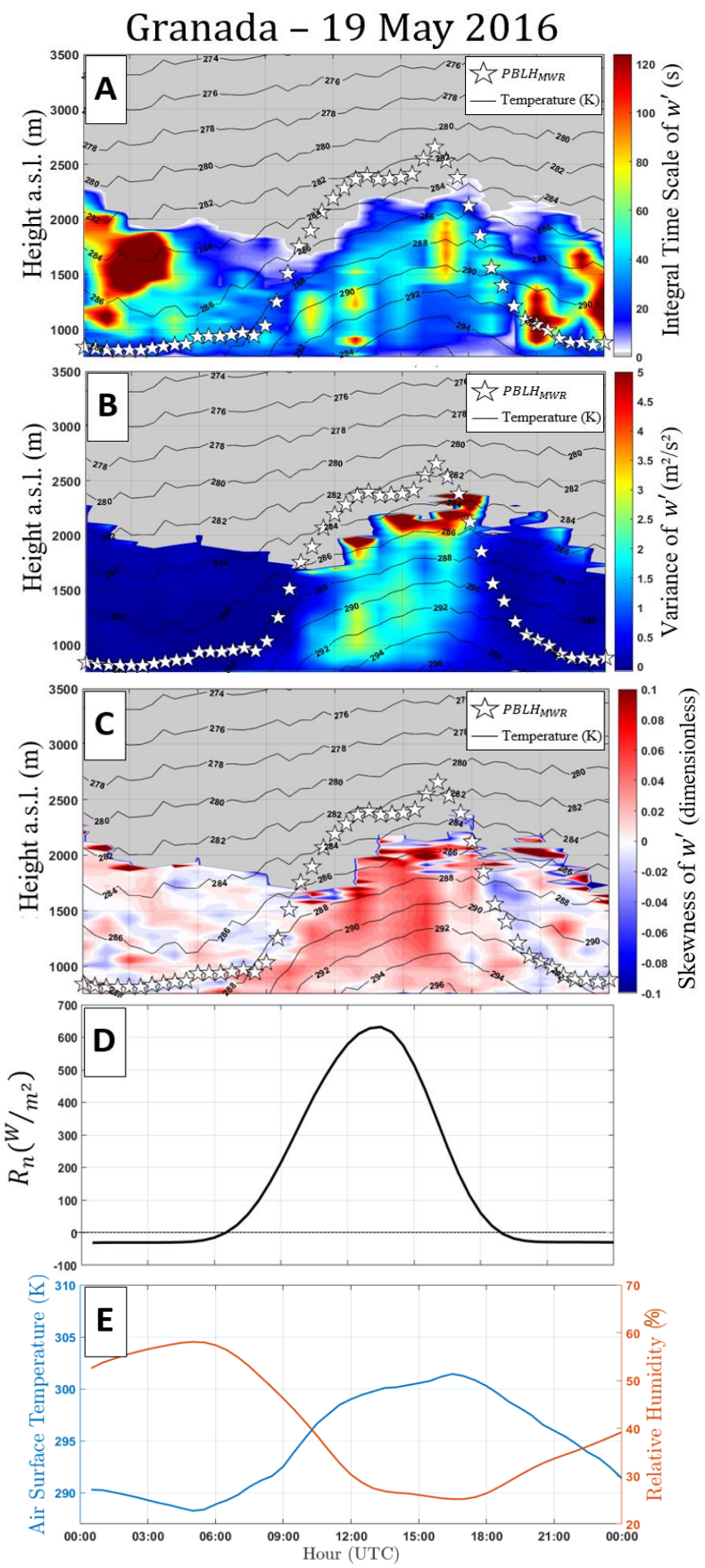

Figure 11 – A – integral time scale obtained from Doppler lidar data [$\boldsymbol{\tau_{w'}}$], B – variance obtained from Doppler lidar data [$\boldsymbol{\sigma^2_{w'}}$], C – skewness obtained from Doppler lidar data [$\boldsymbol{S_{w'}}$], D – net radiation obtained from pyranometer data [R_n], E – Air surface temperature [blue line] and surface relative humidity [RH - orange line] both were obtained from surface sensors. All profiles were acquired on 19th May 2016 in Granada. In A, B and C black lines and white stars represent air temperature and $PBLH_{MWR}$, respectively.

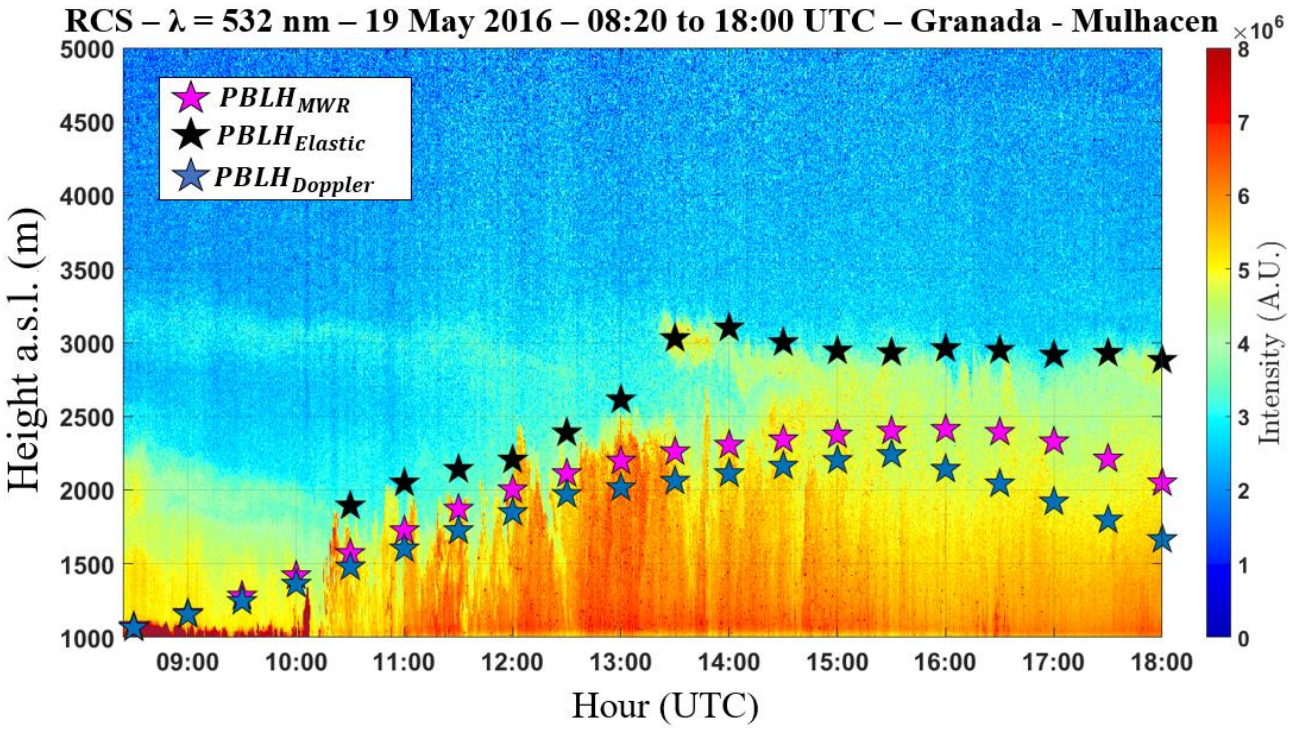

Figure 12 – Time-Height plot of RCS obtained on 19 May 2016 in Granada. Pink stars represent the $PBLH_{MWR}$, black stars represent the $PBLH_{Elastic}$ and blues stars represent the $PBLH_{Doppler}$.

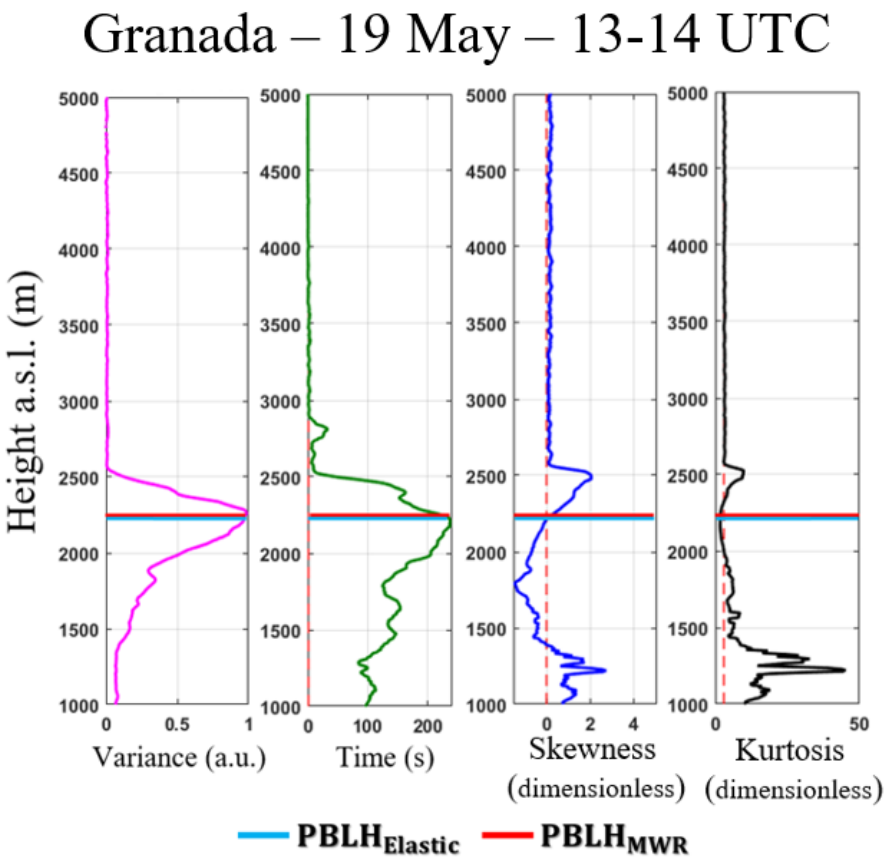

Figure 13 – Statistical moments obtained from 532 nm wavelength data of elastic lidar (Mulhacen) in Granada at 13 to 14 UTC - 19 May 2016. From left to right: variance [$\boldsymbol{\sigma^2_{RCS'}}$], integral time scale [$\boldsymbol{\tau_{RCS'}}$], skewness [$\boldsymbol{S_{RCS'}}$] and kurtosis [$\boldsymbol{K_{RCS'}}$].

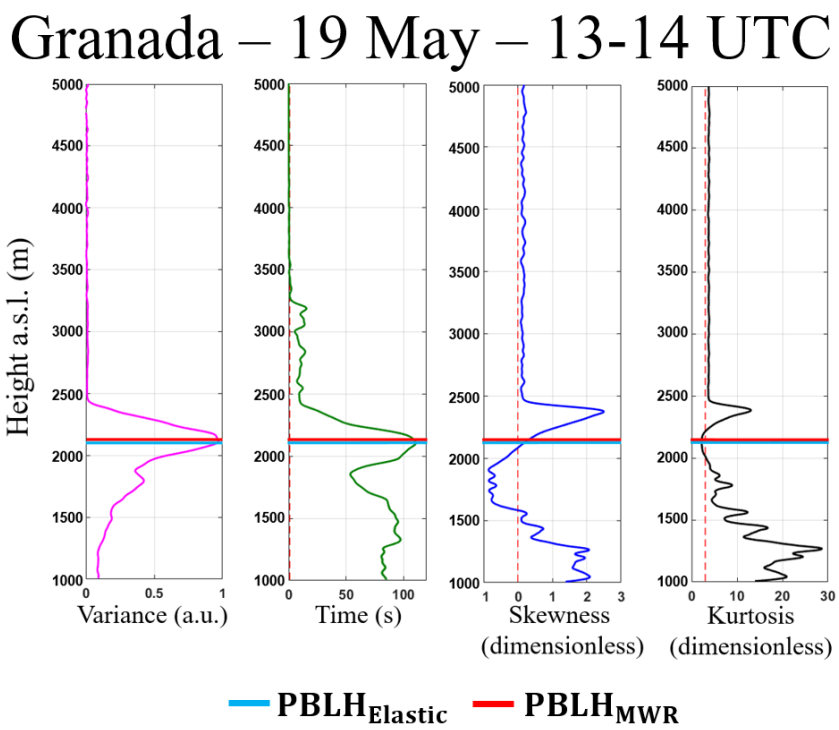

Figure 14 – Statistical moments obtained from 1064 nm wavelength data of elastic lidar(Mulhacen) in Granada at 13 to 14 UTC - 19 May 2016. From left to right: variance [$\boldsymbol{\sigma^2_{RCS'}}$], integral time scale [$\boldsymbol{\tau_{RCS'}}$], skewness [$\boldsymbol{S_{RCS'}}$] and kurtosis [$\boldsymbol{K_{RCS'}}$].

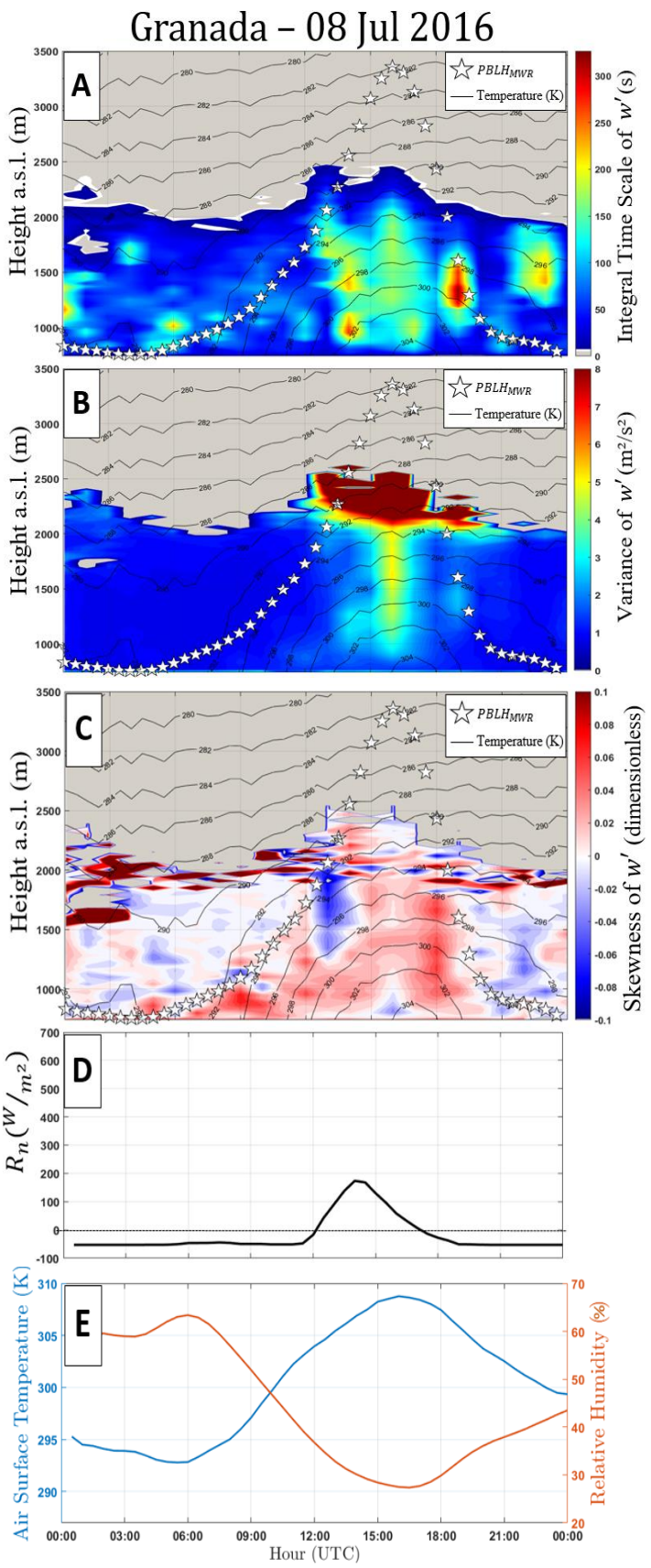

Figure 15 - A – integral time scale from Doppler lidar data [$\boldsymbol{\tau_{w'}}$], B – variance from Doppler lidar data [$\boldsymbol{\sigma^2_{w'}}$], C – skewness from Doppler lidar data [$\boldsymbol{S_{w'}}$], D – net radiation from pyranometer data [R_n], E – Air surface temperature [blue line] and surface relative humidity [RH – orange line] from surface sensor data. All profiles were obtained in Granada on 08 July 2016. In A, B and C black lines and white stars represent air temperature and $PBLH_{MWR}$, respectively.

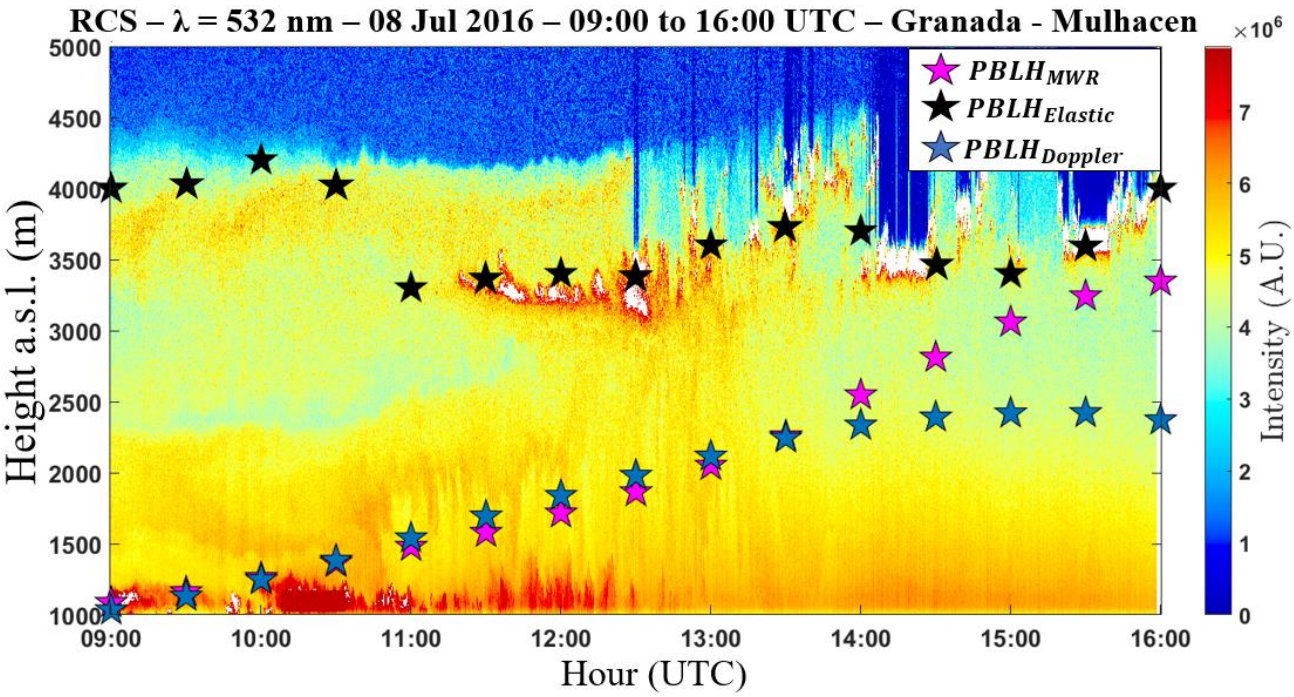

Figure 16 – Time-Height plot of RCS obtained from Mulhacen elastic lidar data on 08 July 2016 in Granada. Pink stars represent the $PBLH_{MWR}$, black stars represent the $PBLH_{Elastic}$ and blues stars represent the $PBLH_{Doppler}$.

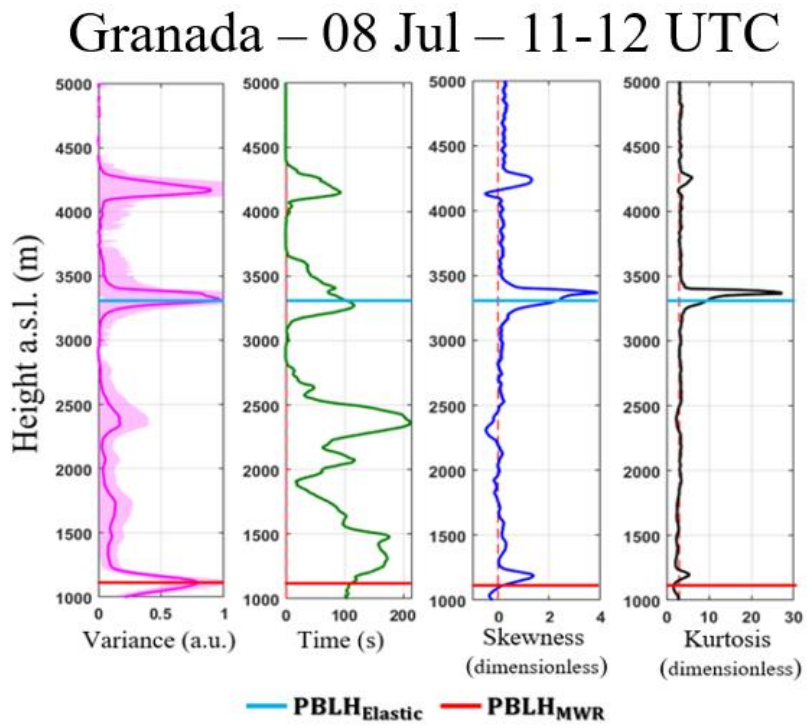

Figure 17 - Statistical moments obtained from 532 nm wavelength data of elastic lidar(Mulhacen) in Granada between 11-12 UTC on 08th July 2016. From left to right: variance [$\sigma^2_{RCS'}$], integral time scale [$\tau_{RCS'}$], skewness [$S_{RCS'}$] and kurtosis [$K_{RCS'}$].

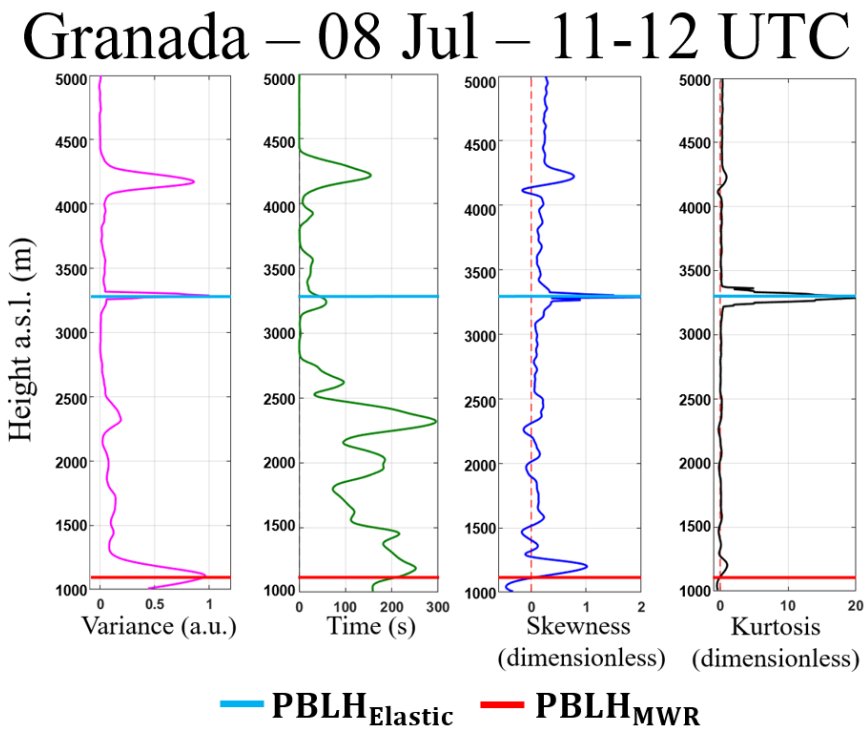

Figure 18 - Statistical moments obtained from 1064 nm wavelength data of elastic lidar(Mulhacen) in Granada between 11-12 UTC on 08th July 2016. From left to right: variance [$\sigma^2_{RCS'}$], integral time scale [$\tau_{RCS'}$], skewness [$S_{RCS'}$] and kurtosis [$K_{RCS'}$].

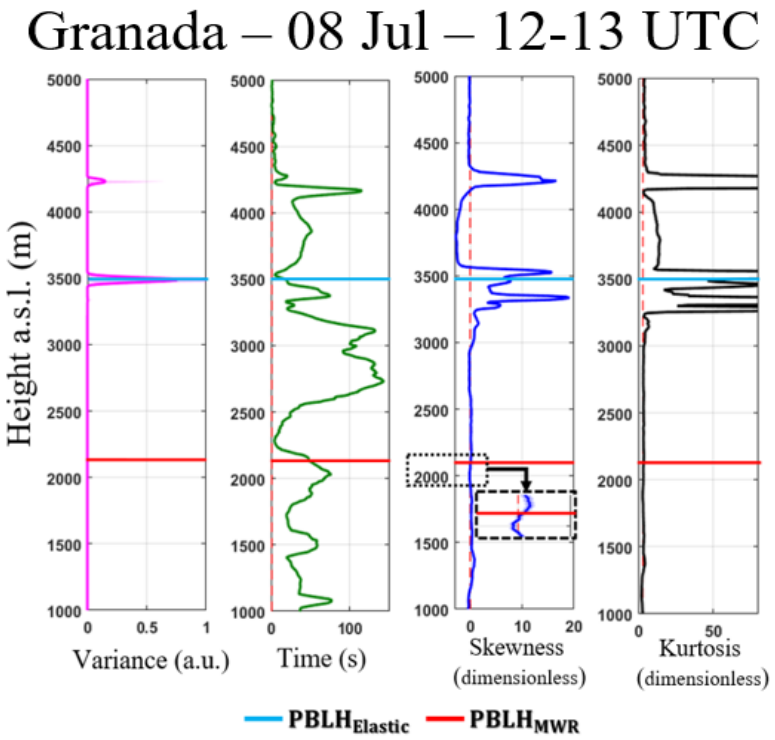

Figure 19 - Statistical moments obtained from 532 nm wavelength data of elastic lidar (Mulhacen) in Granada between 12 -13 UTC on 08 July 2016. From left to right: variance [$\boldsymbol{\sigma^2_{RCS'}}$], integral time scale [$\boldsymbol{\tau_{RCS'}}$], skewness [$\boldsymbol{S_{RCS'}}$] and kurtosis [$\boldsymbol{K_{RCS'}}$].

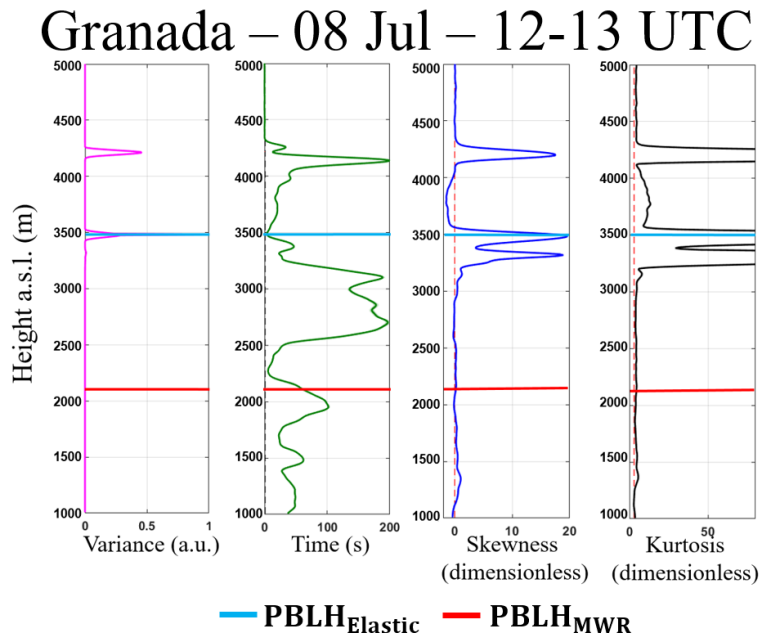

Figure 20 - Statistical moments obtained from 1064 nm wavelength data of elastic lidar (Mulhacen) in Granada between 12 -13 UTC on 08 July 2016. From left to right: variance [$\boldsymbol{\sigma^2_{RCS'}}$], integral time scale [$\boldsymbol{\tau_{RCS'}}$], skewness [$\boldsymbol{S_{RCS'}}$] and kurtosis [$\boldsymbol{K_{RCS'}}$].